Materials Advances

ROYAL SOCIETY OF CHEMISTRY

PAPER

View Article Online
View Journal

Cite this: DOI: 10.1039/d6ma00106h

Computational assessment of structural, mechanical, and thermal properties of ordered MAX phases V_2ZrSiC_2 and Ti_2ZrSiC_2 for high-temperature applications

Mohammed Traiche,[a] Md. Nurul Amin, *[b] Ahmed Azzouz-Rached,[c] M. A. Ali,[b] Tasneem Alayed,[d] Aya M. Al-Zuheiri,[e] Yazen M. Alawaideh,[f] Abdulla Al Faysal[b] and M. S. Alam[g]

Chemically ordered quaternary MAX phases offer a route to tailor stiffness, anisotropy, and transport in layered carbides. Using all-electron FP-LAPW DFT (GGA-PBE), we investigate V_2ZrSiC_2 and Ti_2ZrSiC_2 in α- and β-stacking variants. EOS fits show strong stacking sensitivity: α polytypes are stiffer (bulk moduli ~216 GPa for V_2ZrSiC_2 and ~192 GPa for Ti_2ZrSiC_2) than β polytypes (~178 and ~157 GPa). Elastic constants satisfy the Born criteria, and VRH averages indicate higher shear/tensile rigidity and hardness for Ti_2ZrSiC_2 ($G \approx 136$ GPa, $E \approx 328$ GPa, and $H_V \approx 21$ GPa) than that for V_2ZrSiC_2 ($G \approx 121$ GPa, $E \approx 305$ GPa, and $H_V \approx 14$ GPa), while V_2ZrSiC_2 retains higher incompressibility ($B \approx 214$ GPa). Both phases are metallic with transition-metal d states dominating near E_F, and phonon dispersions show no imaginary modes along the sampled path. Quasi-harmonic Debye–Grüneisen results yield $\Theta_D \sim 669$ K (V_2ZrSiC_2) and ~726 K (Ti_2ZrSiC_2); Slack-type estimates give $k_{ph} \sim 10$–11 W m^{-1} K^{-1} at 300 K with an approximate $1/T$ decrease. The computed linear CTE at 1300 K ($\alpha_L \approx 0.95$ and 1.06×10^{-5} K^{-1}) lies between those of representative α-Al_2O_3 and YSZ, suggesting screening-level thermo-expansion compatibility for coating-stack layers. Energies above the convex hull are $\Delta E_{hull} \sim 0.10$–$0.19$ eV per atom, indicating metastability at $T = 0$ K with respect to competing phases and motivating further synthesis-focused thermodynamic analysis alongside oxidation and interface-stability assessment.

Received 23rd January 2026,
Accepted 14th March 2026

DOI: 10.1039/d6ma00106h

rsc.li/materials-advances

1 Introduction

Materials that retain strength, functional electrical/thermal transport, and damage tolerance under severe thermal and mechanical loading are central to advanced energy technologies and protective-coating systems. Among candidate material classes, the MAX phases, a family of layered carbides and nitrides with the general formula $M_{n+1}AX_n$ (n = 1, 2, 3, ...), are distinctive because they combine ceramic-like and metallic-like characteristics within a single crystalline architecture.[1–3] Here, M is an early transition metal, A is typically a group 13–16 element, and X is commonly C or N. Most MAX phases crystallize in the hexagonal $P6_3/mmc$ structure, where close-packed M layers alternate with comparatively metallic A layers and strongly bonded M–X slabs, producing a nanolaminated solid with anisotropic bonding.[1,3] Following early reports on layered carbide prototypes,[4] the MAX family has expanded substantially in both chemistry and accessible property space.[2,3]

This layered bonding topology underpins the well-known hybrid property set of MAX phases: high stiffness and thermal stability alongside good electrical/thermal conductivity, machinability, and damage tolerance.[5–7] Complementing extensive experimental work, density functional theory (DFT) studies have been central for mapping stability windows and property trends across composition space, including elastic anisotropy, electronic structure, and thermodynamic indicators.[8–12] As a result, MAX phases are broadly viewed as tunable platforms where chemistry and layered bonding can be engineered to reconcile thermal robustness with functional transport.[2,3]

These characteristics motivate interest in MAX phases for high-temperature structural components and multifunctional

[a] Department of Common Core Science and Technology, Faculty of Technology, Hassiba BENBOUALI University of Chlef, Chlef, Algeria
[b] Department of Physics, Chittagong University of Engineering and Technology (CUET), Chattogram-4349, Bangladesh. E-mail: nurulaminarju@gmail.com
[c] Department of Physics, Faculty of Sciences, University Saad Dahlab Blida 1, Blida, Algeria
[d] Department of Basic Sciences, Faculty of Science, Applied Science Private University, Amman 11931, Jordan
[e] Department of Basic Sciences, Middle East University, Amman 11831, Jordan
[f] MEU Research Unit, Middle East University, Amman, Jordan
[g] Department of Physics, University of Chittagong, Chattogram 4331, Bangladesh

protective coatings and also as parent materials for two-dimensional MXenes formed by selective etching of the A layers.[3,13,14] Advances in synthesis, thin-film growth, and composition design have expanded the palette of achievable MAX chemistries and microstructures, strengthening the case for application-driven screening strategies.[15] In coating-relevant settings, combining oxidation resistance, thermal-shock tolerance, and electrical/thermal conduction is attractive for multilayer architectures that protect substrates while maintaining functional performance.[6,7] In thermal-barrier coating (TBC) concepts, performance is governed by architecture: a compliant, oxidation-resistant, and thermally compatible layer can improve adhesion and limit damage accumulation during high-temperature exposure. High-temperature durability studies of YSZ coatings on MAX-phase substrates illustrate this architectural role: YSZ layers ($\sim$80–100 μm) have been evaluated under stepped, interrupted furnace exposures spanning 1100–1300 °C (hundreds of hours at each temperature), showing that Ti_2AlC-based systems can maintain coating integrity up to 1300 °C, whereas Cr_2AlC-based systems exhibit earlier failure under comparable conditions.[16] These observations motivate continued exploration of MAX chemistries as conductive and thermally robust layers within coating stacks. At the same time, key TBC-lifetime drivers, oxidation thermodynamics, thermally grown oxide (TGO) evolution, and interfacial phase equilibria with common constituents (*e.g.*, YSZ and Al_2O_3), are system-specific and must be evaluated explicitly for any proposed chemistry.

Beyond conventional ternary MAX phases, chemically ordered double-transition-metal (ordered or quaternary) MAX phases add a further degree of freedom by placing two different transition metals on distinct M sublattices, commonly written as $M_2M'AX_2$.[17,18] This site selectivity can reshape bonding anisotropy, modify elastic and transport responses, and alter polymorph/stacking preferences.[17,18] For example, the ordered MAX phase $(Cr_{2/3}Ti_{1/3})_3AlC_2$ was established through combined experimental characterization and first-principles analysis, illustrating how chemical order can suppress competing distortions and stabilize the layered structure.[19] More broadly, first-principles screening suggests that ordered MAX phases can be tuned for both mechanical robustness and functional behavior, reinforcing their value as a design space for targeted applications.[20] Recent computational work has also discussed ordered MAX phases in coating-related concepts, where thermo-mechanical compatibility and controlled heat transport are central.[21,22]

Zr-containing MAX phases are compelling for extreme environments because Zr can modify oxidation behavior and irradiation tolerance while preserving the layered MAX crystal chemistry.[23,24] First-principles studies of Zr-bearing compositions and predictions of new Zr-based ordered compounds indicate that Zr substitution can substantially alter bonding and elastic response.[25,26] Progress in processing also matters: spark plasma sintering (SPS) has enabled synthesis and property assessment of additional chemistries (including In-containing MAX phases), providing benchmarks for transport and thermodynamic behavior under demanding conditions.[27] In parallel, MAX-phase design has expanded toward harsh-environments and nuclear-relevant concepts (including Sn-based proposals), emphasizing the continuing need for reliable thermo-mechanical datasets across emerging compositions.[28]

The broader coating landscape further reinforces the need for predictive structure–property links. Layered and MAX-derived compositions (including boride- or B-containing variants and hypothetical layered analogues) have been examined computationally for stability and lattice dynamics,[29–31] while experimentally oriented coating research has advanced thermal-spray and composite strategies for erosion-corrosion and wear reduction.[32–35] Data-driven approaches (including machine learning) are increasingly used to accelerate coating discovery by screening complex performance metrics, such as ablation resistance, and complementing physics-based calculations and targeted experiments.[36,37] Across these themes, defects and microstructural complexity remain central: stacking faults, dislocations, and vacancies can strongly influence oxidation and reliability in MAX phases and their derivatives, motivating a combined focus on intrinsic bonding and lattice stability.[38,39]

From a modeling standpoint, DFT is indispensable for comparing equilibrium structures, elastic constants, and electronic structures, while lattice-dynamical calculations provide a direct test of dynamical stability and connect bonding stiffness to vibrational spectra and thermal trends.[8,11,40] Building on these ideas, the present work reports a first-principles assessment of the chemically ordered quaternary MAX phases V_2ZrSiC_2 and Ti_2ZrSiC_2 in both α- and β-stacking variants. The specific contributions of this study are as follows: (i) quantifying stacking-dependent compressibility and elastic anisotropy using all-electron FP-LAPW calculations; (ii) establishing harmonic dynamical stability *via* phonon dispersions; (iii) comparing metallic electronic structure and Fermi-level descriptors relevant to transport; and (iv) providing finite-temperature thermoelastic and free-energy trends within a quasi-harmonic Debye–Grüneisen treatment (Gibbs2), including $V(T,P)$, $\Theta_D(T,P)$, $\alpha(T,P)$, $C_V(T,P)$, $G(T,P)$ and $F_{vib}(T,P)$. Altogether, these results provide a coherent thermo-mechanical and transport dataset for Zr-containing ordered MAX phases and motivate their screening-level consideration as conductive, thermally compatible layers in coating architectures, while emphasizing that oxidation resistance, interfacial phase stability, and full competing-phase (convex-hull) thermodynamic stability require dedicated evaluation beyond the scope of the present work.[21–24]

2 Computational methods

All calculations were performed within Kohn–Sham density functional theory using the full-potential linearized augmented plane-wave (FP-LAPW) method.[40,41] The FP-LAPW formalism, as implemented in the WIEN2k package,[42–44] was used to determine the structural, elastic, electronic, and thermodynamic properties of the chemically ordered MAX phases and their stacking variants. Exchange–correlation effects were treated within the generalized gradient approximation of

Perdew–Burke–Ernzerhof (GGA-PBE).[45] Core and valence states were separated using the standard WIEN2k criterion, and self-consistency was enforced with tight numerical tolerances to ensure well-converged energies, stresses, and elastic constants.

The LAPW basis size was controlled by $R_{MT}K_{max}$, where R_{MT} is the smallest muffin-tin radius and K_{max} is the plane-wave cutoff. Convergence tests and production calculations used $R_{MT}K_{max} = 7$. Muffin-tin radii were chosen element-by-element (typically ~1.5–2.5 bohr) to avoid sphere overlap. Inside muffin-tin spheres, wave functions were expanded up to $l_{max} = 10$, and the Fourier expansion of the charge density in the interstitial region was truncated at $G_{max} = 14$ a.u.$^{-1}$. Brillouin-zone integrations were performed using a Γ-centered Monkhorst–Pack grid; meshes up to 11 × 11 × 4 were tested and the final mesh was verified to converge total energies and elastic constants. The self-consistent field (SCF) cycles were deemed converged when the total-energy change fell below 1.0×10^{-5} Hartree and the total-charge difference between successive iterations was less than 1.0×10^{-4} e a.u.$^{-3}$. All structures were fully relaxed (lattice parameters and internal coordinates) until the maximum residual force on any atom was below 1 mRy a.u.$^{-1}$.

For each compound and stacking sequence, a variable-cell relaxation was followed by fixed-volume calculations around equilibrium to generate the $E(V)$ dataset. The equation of state was fitted to the third-order Birch–Murnaghan form [eqn (1)] to extract the equilibrium volume V_0, bulk modulus B_0, and its pressure derivative B_0'. Thermodynamic driving forces relative to elemental reference phases were assessed *via* the formation energy per atom using fully relaxed total energies [eqn (2)]. Second-order elastic constants C_{ij} were computed using the Irelast interface within WIEN2k, which applies symmetry-allowed strain patterns and determines C_{ij} from the stress/energy response.[46] Mechanical stability was assessed using the Born criteria for hexagonal crystals, and polycrystalline elastic moduli were obtained using the Voigt–Reuss–Hill averaging scheme.

Dynamical stability was examined by calculating phonon dispersion relations using a finite-displacement (supercell) approach. Symmetry-inequivalent atomic displacements were generated in a 2 × 1 × 2 supercell constructed from the conventional $P6_3/mmc$ cell.[47] The resulting real-space interatomic force constants were Fourier transformed to build the dynamical matrix and obtain phonon frequencies along a representative high-symmetry path in the hexagonal Brillouin zone.

Finite-temperature thermodynamic response functions were evaluated within a quasi-harmonic Debye–Grüneisen (semi-harmonic Debye) framework using the Gibbs2 code,[48] interfaced with the equation-of-state (and, where needed, elastic) data. This approach provides the temperature- and pressure-dependent volume $V(T,P)$, Debye temperature $\Theta_D(T,P)$, thermal expansion coefficient $\alpha(T,P)$, isochoric heat capacity $C_V(T,P)$, and the corresponding Gibbs and vibrational free-energy trends within the Debye-model free-energy formalism. The minimum thermal conductivity k_{min} was estimated using Clarke/Cahill-type scaling, while the lattice thermal conductivity k_{ph} was evaluated using a Slack-like model [eqn (21)] with a Grüneisen parameter obtained consistently within the quasi-harmonic treatment. When relevant, the electronic contribution to thermal transport can be linked to the electrical conductivity *via* the Wiedemann–Franz relation, $\kappa_e = L\sigma T$, adopting the Sommerfeld Lorenz number L_0; in the present work we focus on lattice and thermoelastic indicators derived from the computed elastic, Debye, and phonon descriptors.

3 Results and discussion

3.1 Structural and phase stability

3.1.1 Structural parameters. Fig. 1 illustrates the chemically ordered $M_2M'AX_2$ (312-type, $P6_3/mmc$) framework considered here, in which the transition-metal sublattice is partitioned into distinct M = {V,Ti} and M′ = Zr layers separated by Si and C sublayers. In the conventional hexagonal description, M occupies the 2*a* Wyckoff position (0,0,0), Si resides at 2*b* $\left(0,0,\frac{1}{4}\right)$ for α-stacking and 2d $\left(\frac{2}{3},\frac{1}{3},\frac{1}{4}\right)$ for β-stacking, while Zr and C occupy 4f sites at $\left(\frac{1}{3},\frac{2}{3},z\right)$ with internal coordinates z_{Zr} = 0.13099 and z_C = 0.93416, respectively. These 4f parameters control the separation between Zr and C planes and therefore the thickness of the M–C–M′ slabs and the spacing to the Si layers along the *c* axis.

The optimized lattice parameters (Table 1) reflect the nanolaminated anisotropy typical of MAX phases: the in-plane lattice constants are compact (a = 3.11 Å for V_2ZrSiC_2 and a = 3.18 Å for Ti_2ZrSiC_2 in the α polymorph), whereas the *c* axis is governed by stacking periodicity and interlayer separation, yielding c = 17.24 Å (V_2ZrSiC_2) and c = 18.30 Å (Ti_2ZrSiC_2). The corresponding c/a ratios of 5.54 and 5.75 confirm pronounced structural anisotropy. Between stacking variants, the β polymorphs exhibit notably larger *c* and c/a (Table 1), indicating that changing the stacking registry primarily modifies the interlayer repeat distance along *c* rather than the in-plane metal–carbon network. This geometric change is consistent

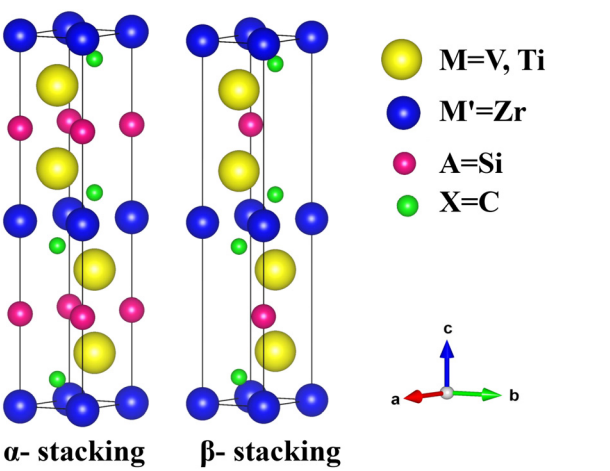

Fig. 1 Chemically ordered crystal structures of the quaternary MAX phases V_2ZrSiC_2 and Ti_2ZrSiC_2 in the hexagonal $P6_3/mmc$ lattice, shown for the α- and β-stacking variants.

Table 1 Optimized structural parameters (a, c, and c/a), Birch–Murnaghan equation-of-state parameters (B_0, B_0'), total energy E_{tot}, elemental formation energy E_{form} (per atom), and energy above the convex hull ΔE_{hull} (per atom) for V_2ZrSiC_2 and Ti_2ZrSiC_2 in the α and β stacking variants

Compound	Ref.	Stack	a (Å)	c (Å)	c/a	B_0 (GPa)	B_0'	E_{tot} (Ry)	E_{form} (eV per atom)	ΔE_{hull} (eV per atom)
V_2ZrSiC_2	This work	α	3.11	17.24	5.54	216.34	4.11	-2.3465×10^4	−0.658	0.137
		β	2.98	21.84	7.31	178.07	4.24	-2.3456×10^4	−0.987	0.162
Ti_2ZrSiC_2	This work	α	3.18	18.30	5.75	191.88	3.98	-2.2693×10^4	−0.987	0.100
		β	3.22	20.29	6.29	156.78	4.10	-2.2692×10^4	−1.365	0.190
V_2ScSnC_2	49	α	3.14	20.41	6.49	154.17	4.21	-4.8535×10^5	−0.093	—
Zr_2TiSiC_2	26	α	3.26	18.52	5.68	184.68	4.01	-4.5816×10^5	−4.702	—

with the strong stacking sensitivity later observed in volumetric stiffness and anisotropy metrics.

Equation-of-state (EOS) fits of the $E(V)$ curves (Fig. 2) yield bulk moduli of B_0 = 216.34 GPa for α-V_2ZrSiC_2 and 191.88 GPa for α-Ti_2ZrSiC_2, whereas the β polymorphs are more compressible with B_0 = 178.07 GPa (V_2ZrSiC_2) and 156.78 GPa (Ti_2ZrSiC_2) (Table 1). Thus, changing the stacking sequence produces a substantial reduction in volumetric rigidity, consistent with the larger c-axis repeat distance of the β variants. The fitted pressure derivatives remain close to $B_0' \approx 4$, as commonly observed for mixed metallic-covalent solids. The $E(V)$ data were fitted to the third-order Birch–Murnaghan equation of state,[50,51]

$$E(V) = E_0 + \frac{9V_0B_0}{16}\{(\eta-1)^3B_0' + (\eta-1)^2(6-4\eta)\}, \quad \eta = \left(\frac{V_0}{V}\right)^{2/3}, \tag{1}$$

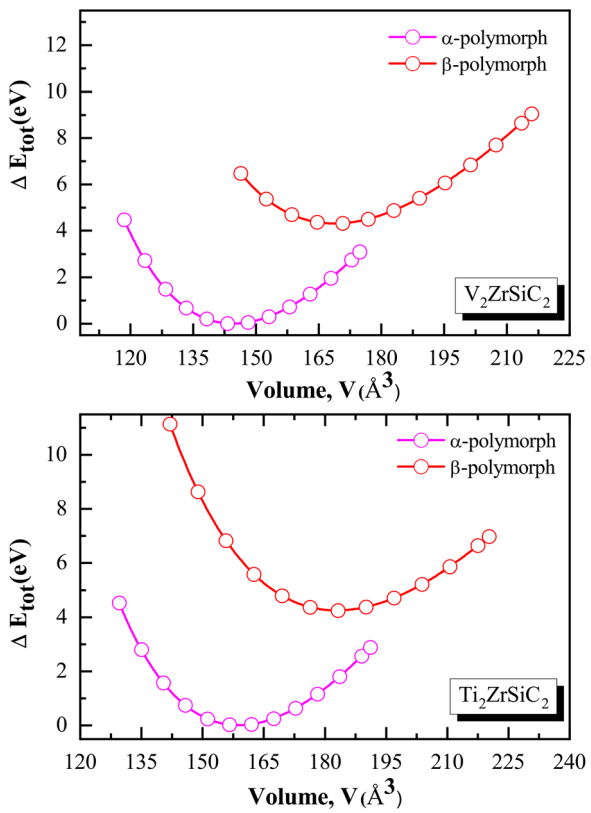

Fig. 2 Total energy *versus* volume, $E(V)$, for V_2ZrSiC_2 and Ti_2ZrSiC_2 in the α and β stacking variants.

where $E(V)$ is the total energy at volume V, E_0 and V_0 are the equilibrium energy and volume, B_0 is the bulk modulus at V_0, B_0' is its first pressure derivative, and η is the Eulerian finite strain. The relative positions of the minima in Fig. 2 indicate that the α stacking is energetically preferred over the β polymorphs for both V_2ZrSiC_2 and Ti_2ZrSiC_2 within the present calculations.

Relative to the comparison entries in Table 1, the in-plane lattice constants of V_2ZrSiC_2 and Ti_2ZrSiC_2 are close to that of V_2ScSnC_2,[49] while their c parameters are smaller in the α polytypes, reflecting differences in layer chemistry and stacking periodicity. The EOS bulk moduli of the present Zr-containing quaternaries are substantially higher than that of V_2ScSnC_2[49] and are comparable to or exceed that of Zr_2TiSiC_2,[26] underscoring strong resistance to volume compression in these chemically ordered laminates. In particular, the large α–β stiffness difference indicates that stacking registry provides a meaningful design lever to tune compressibility in ordered MAX phases without changing overall composition.

3.1.2 Formation energy and thermodynamic stability. To assess thermodynamic driving forces relative to the constituent elements, we evaluated the elemental formation energy per atom as[52,53]

$$E_{form} = \frac{E_{tot}(M_2ZrSiC_2) - 2\mu_M - \mu_{Zr} - \mu_{Si} - 2\mu_C}{N_{atoms}}, \tag{2}$$

where $E_{tot}(M_2ZrSiC_2)$ is the fully relaxed total energy of the ordered MAX phase (M = V or Ti), μ_i are elemental reference chemical potentials ($i \in$ {M, Zr, Si, C}), and N_{atoms} is the number of atoms in the simulation cell. The calculated E_{form} values in Table 1 are negative for both compositions and stacking variants, indicating a thermodynamic driving force with respect to decomposition into the elemental reference states within the present convention.

For multicomponent MAX phases, however, negative elemental formation energies are a necessary but not sufficient condition for synthesizability. A more stringent metric is the convex-hull energy (energy above hull), which measures stability against decomposition into the lowest-energy set of competing phases at the same overall composition. The (per-atom) energy above the convex hull is written as

$$\Delta E_{hull} = E_{tot}^{atom}(M_2ZrSiC_2) - \min_{\{x_i\}}\left(\sum_i x_i E_i^{atom}\right), \quad \text{s.t.} \sum_i x_i \mathbf{c}_i = \mathbf{c}_{target}, \quad x_i \geq 0, \tag{3}$$

where $E_{\mathrm{tot}}^{\mathrm{atom}}$ is the total energy per atom of the target phase, E_i^{atom} are the energies per atom of competing phases i, x_i are nonnegative phase fractions, and $\mathbf{c}$ denotes the composition vector. By construction, $\Delta E_{\mathrm{hull}} = 0$ corresponds to a phase on the convex hull, while $\Delta E_{\mathrm{hull}} > 0$ indicates metastability at $T = 0$ K within the chosen competing-phase set.

The calculated ΔE_{hull} values (Table 1) fall in the range ~0.10–0.19 eV per atom for the investigated stackings, indicating metastability with respect to competing phases at $T = 0$ K in the present hull construction. Such metastable layered carbides can still be experimentally accessible due to kinetic stabilization and non-equilibrium processing routes (*e.g.*, rapid densification/sintering and thin-film growth), and finite-temperature vibrational entropy can reduce the free-energy driving force for decomposition.

For comparison, the Open Quantum Materials Database (OQMD) reports decomposition products for the same chemistries and provides an associated decomposition/reaction enthalpy measure.[53] The OQMD-reported decomposition reactions are

$$V_2ZrSiC_2 \rightarrow SiC + ZrC + V_6C_5 + ZrSi, \quad \Delta H_{\mathrm{OQMD}} = -0.638 \text{ eV per atom} \tag{4}$$

and

$$Ti_2ZrSiC_2 \rightarrow TiC + ZrSi, \quad \Delta H_{\mathrm{OQMD}} = -0.848 \text{ eV per atom.} \tag{5}$$

While ΔH_{OQMD} and ΔE_{hull} are not identical quantities (they can differ in reference conventions, competing-phase sets, and definitions used in database hull constructions), both analyses indicate that competing-phase energetics must be considered beyond elemental formation energies. In our calculations, the positive energies above hull (ΔE_{hull} ~ 0.10–0.19 eV per atom; Table 1) support the interpretation that these ordered MAX structures are metastable at $T = 0$ K with respect to the adopted competing phases, motivating further stability validation using a comprehensive competing-phase set (and, ideally, finite-temperature competing-phase free energies) in the full Ti–Zr–Si–C and V–Zr–Si–C spaces.

Within a fixed composition, the relative stability of stacking variants is most robustly inferred from relative total energies computed under identical settings. Using the EOS minima in Fig. 2 and the corresponding total energies in Table 1, we identify the preferred stacking in the present FP-LAPW calculations: the α stacking is lower in energy than the β variant for both V_2ZrSiC_2 and Ti_2ZrSiC_2. In addition to static (T = 0 K) energetics, finite-temperature vibrational contributions can modify free-energy trends; accordingly, Section 3.4 reports Gibbs and vibrational free-energy trends within the Debye–Grüneisen framework to provide a complementary finite-T perspective for the assumed MAX-phase structures.

3.1.3 Phonon dispersion and dynamical stability. To assess dynamical stability of the predicted quaternary MAX phases, we calculated harmonic phonon dispersion relations across the Brillouin zone. Within the harmonic approximation, phonon frequencies are obtained by solving the dynamical-matrix eigenvalue problem[47]

$$\sum_{\kappa',\beta} D_{\alpha\beta}^{\kappa\kappa'}(\mathbf{q}) e_{\beta}^{\kappa'}(\mathbf{q}j) = \omega^2(\mathbf{q}j) e_{\alpha}^{\kappa}(\mathbf{q}j), \tag{6}$$

where $\mathbf{q}$ is the phonon wave vector, j labels the phonon branch, $\omega(\mathbf{q}j)$ is the phonon angular frequency, $e_{\alpha}^{\kappa}(\mathbf{q}j)$ is the polarization vector of atom κ for Cartesian component α, and $D_{\alpha\beta}^{\kappa\kappa'}(\mathbf{q})$ is the dynamical matrix. In reciprocal space, $D_{\alpha\beta}^{\kappa\kappa'}(\mathbf{q})$ is constructed from the real-space interatomic force constants (IFCs) $\Phi_{\alpha\beta}(\kappa 0, \kappa' l)$ as[47]

$$D_{\alpha\beta}^{\kappa\kappa'}(\mathbf{q}) = \frac{1}{\sqrt{m_\kappa m_{\kappa'}}} \sum_l \Phi_{\alpha\beta}(\kappa 0, \kappa' l) \exp[i\mathbf{q} \cdot (\mathbf{R}_l + \tau_{\kappa'} - \tau_\kappa)], \tag{7}$$

where m_κ is the atomic mass, $\mathbf{R}_l$ is a lattice translation vector, and τ_κ denotes the basis vector of atom κ in the unit cell. A crystal is dynamically stable if $\omega^2(\mathbf{q}j) > 0$ for all branches and all $\mathbf{q}$, *i.e.*, the phonon spectrum contains no imaginary frequencies.

As shown in Fig. 3, both V_2ZrSiC_2 and Ti_2ZrSiC_2 exhibit nonnegative phonon frequencies throughout the sampled high-symmetry path, indicating harmonic dynamical stability of the optimized structures at 0 K. The acoustic branches display the expected linear behavior near Γ, consistent with well-defined elastic-wave propagation. No optical branches soften toward 0 THz at the zone-boundary points (A, H, K, M, or L), suggesting no tendency toward symmetry-lowering distortions along these directions. The spectra extend to approximately ~20 THz for both compounds, and the total phonon DOS shows pronounced contributions in the low-to-intermediate frequency range (where heavier transition-metal/Zr motions dominate) together with higher-frequency optical features associated with the lighter C sublattice and stiff M–C bonding.

The absence of imaginary phonon modes provides a necessary baseline for the quasi-harmonic thermodynamic trends discussed in Section 3.4. It should be emphasized that harmonic dynamical stability is distinct from competing-phase thermodynamic stability: even if a structure is dynamically stable, establishing synthesizability requires an explicit assessment against alternative Ti–Zr–Si–C and V–Zr–Si–C phases (*e.g.*, *via* convex-hull analysis) and, where relevant, finite-temperature phase equilibria.

3.2 Elastic properties

The single-crystal elastic constants C_{ij} provide the primary mechanical descriptors of hexagonal MAX phases. Hexagonal crystals are mechanically stable when they satisfy the Born criteria:[54–56] $C_{11} > |C_{12}|$, $C_{44} > 0$, $C_{66} = \frac{1}{2}(C_{11} - C_{12}) > 0$, and $(C_{11} + 2C_{12})C_{33} > 2C_{13}^2$, where C_{ij} are the elastic constants in Voigt notation (GPa).

All calculated constants for V_2ZrSiC_2 and Ti_2ZrSiC_2 in Table 2 satisfy the Born criteria, confirming mechanical stability. Both compounds exhibit large axial stiffness ($C_{33} > C_{11}$),

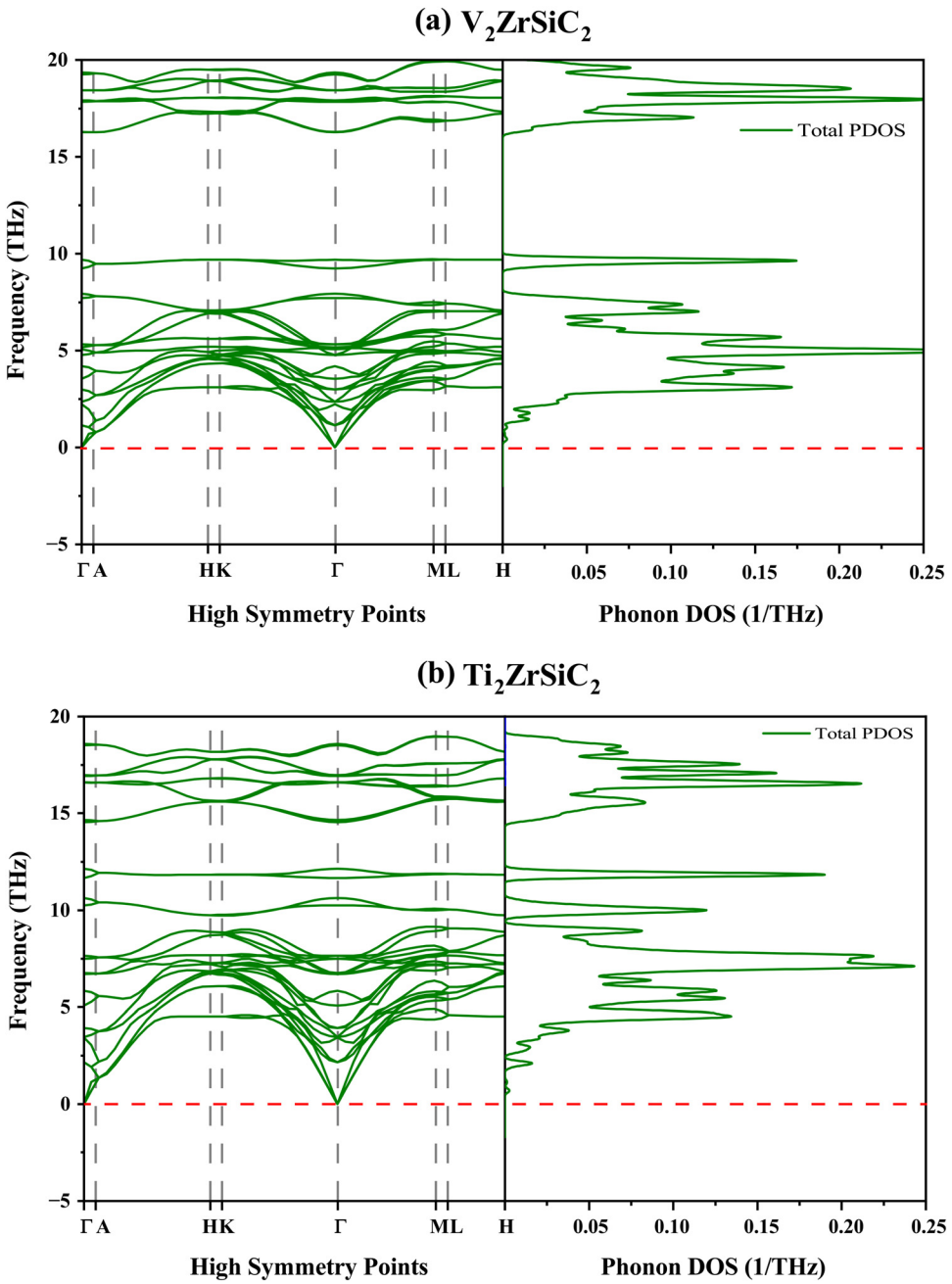

Fig. 3 Phonon dispersion relations (left) and total phonon density of states (right) for (a) V_2ZrSiC_2 and (b) Ti_2ZrSiC_2 along the hexagonal high-symmetry path Γ–A–H–K–Γ–M–L–H.

Table 2 Computed single-crystal elastic constants C_{ij} (GPa) for V_2ZrSiC_2 and Ti_2ZrSiC_2

Compound		C_{11}	C_{33}	C_{12}	C_{13}	C_{44}	C_{66}
V_2ZrSiC_2	This work	329.08	347.82	130.45	165.88	178.29	99.31
Ti_2ZrSiC_2	This work	338.79	372.18	88.43	117.46	158.98	125.17
V_2ScSnC_2	49	288.00	209.00	112.00	104.00	89.00	88.00
Zr_2TiSiC_2	26	333.00	358.00	89.00	113.00	157.00	121.00

indicating strong resistance to deformation along the c direction. Relative to V_2ScSnC_2,[49] the present Zr-containing phases show substantially higher C_{33} and C_{44}, reflecting enhanced resistance to uniaxial compression and shear. Their stiffness is comparable to Zr_2TiSiC_2,[26] with Ti_2ZrSiC_2 showing the largest C_{11} and C_{33} among the listed entries.

To compare compounds on an equal footing and connect elastic response with screening-level mechanical indicators, we employ Voigt–Reuss–Hill (VRH) averaging.[57–59] For hexagonal symmetry, the Voigt bounds are $B_V = \{2(C_{11} + C_{12}) + C_{33} + 4C_{13}\}/9$ and $G_V = \{C_{11} + C_{12} + 2C_{33} - 4C_{13} + 12C_{44} + 6(C_{11} - C_{12})\}/30$. The Reuss bounds are obtained from the elastic compliances S_{ij} (inverse of the stiffness matrix) as

$B_R = [2(S_{11} + S_{12}) + 4S_{13} + S_{33}]^{-1}$ and $G_R = 15/\{4(2S_{11} + S_{33}) - 4(S_{12} + 2S_{13}) + 3(2S_{44} + S_{66})\}$.

The Hill averages and related isotropic descriptors are then

$$B = \frac{1}{2}(B_V + B_R), \quad G = \frac{1}{2}(G_V + G_R), \quad E = \frac{9BG}{3B + G}, \quad \nu = \frac{3B - 2G}{2(3B + G)}. \tag{8}$$

Table 3 shows that V_2ZrSiC_2 is the less compressible of the two targets ($B \approx 214$ GPa), consistent with its larger EOS bulk modulus, whereas Ti_2ZrSiC_2 exhibits higher shear rigidity ($G \approx 136$ GPa) and Young's modulus ($E \approx 328$ GPa), indicating greater resistance to shape change. The Pugh ratio further differentiates ductility trends: V_2ZrSiC_2 ($G/B \approx 0.56$) lies near the conventional ductile-brittle boundary, while Ti_2ZrSiC_2 ($G/B \approx 0.72$) lies in the brittle regime, comparable to Zr_2TiSiC_2.[26] Relative to V_2ScSnC_2,[49] both Zr-containing phases show markedly larger B, G, and E, reflecting a stiffer transition-metal–carbon framework.

Vickers hardness was estimated using the Tian empirical relation,[60] $H_V = 2[(k^2G)]^{0.585} - 3$, where H_V is in GPa, $k = G/B$, and G is the Hill shear modulus (GPa). The resulting estimates indicate that Ti_2ZrSiC_2 is substantially harder ($H_V \approx 21$ GPa) than V_2ZrSiC_2 ($H_V \approx 14$ GPa). As with other empirical hardness relations, this estimate is used here as a consistent screening metric and is not a substitute for microstructure-dependent experimental hardness.

Directional Cauchy pressures provide a qualitative indicator of central-force *versus* angular (directional) bonding character.[49,61] For hexagonal crystals, common forms are

$$P_a^{\text{Cauchy}} = C_{12} - C_{44}, \quad P_c^{\text{Cauchy}} = C_{13} - C_{44}. \tag{9}$$

In Table 3, both compounds yield negative P_a^{Cauchy} and P_c^{Cauchy}, consistent with directional bonding contributions in the load-bearing M–C framework; the more negative values for Ti_2ZrSiC_2 are consistent with its lower Poisson's ratio and higher hardness estimate.

Shear anisotropy on the principal planes and the ratio of linear compressibilities[62] are evaluated as

$$A_1 = \frac{C_{11} + C_{12} + 2C_{33} - 4C_{13}}{6C_{44}}, \quad A_2 = \frac{2C_{44}}{C_{11} - C_{12}}, \quad A_3 = \frac{C_{11} + C_{12} + 2C_{33} - 4C_{13}}{3(C_{11} - C_{12})}, \tag{10}$$

$$\frac{k_c}{k_a} = \frac{C_{11} + C_{12} - 2C_{13}}{C_{33} - C_{13}}, \tag{11}$$

where A_1, A_2, and A_3 are dimensionless and k_a and k_c are the linear compressibilities along a and c (GPa^{-1}).

To further relate stiffness to screening-level damage-tolerance and elastic-wave descriptors, we estimated fracture toughness, brittleness index, acoustic impedance, and radiation intensity using elastic-modulus-based relations. The fracture toughness was estimated as $K_{IC} = V_{atom}^{1/6}\sqrt{BG}$, and the brittleness index as $M_B = H_V/K_{IC}$.[63] Acoustic impedance and radiation intensity were evaluated as $Z = \sqrt{\rho G}$ and $I = \sqrt{G/\rho^3}$, where ρ is the density.

The anisotropy factors in Table 4 deviate from unity for both compounds, confirming elastically anisotropic behavior consistent with their layered crystal chemistry. The ratios $k_c/k_a < 1$ imply that the c axis is more compressible than the a axis for the present Zr-containing phases, consistent with nanolaminated bonding in which the interlayer direction is comparatively more compliant. In chemically ordered MAX phases, such anisotropy is sensitive to how the two transition metals partition between distinct M layers, since this modifies the local M–C stiffness and the interlayer registry that primarily governs C_{13}- and C_{44}-related responses.

In layered coating stacks, thermo-mechanical compatibility is often as important as intrinsic stiffness because mismatch strains can drive cracking and spallation during thermal cycling. High-temperature studies of YSZ coatings on alumina-forming MAX substrates emphasize that improved compatibility between the MAX layer and the thermally grown alumina (TGO) can reduce mismatch stresses and delay failure compared with conventional metallic bond-coat systems.[16] In this context, the combination of high stiffness (Tables 2 and 3), moderate elastic anisotropy (Table 4), and bonding/ductility indicators (Cauchy pressures and G/B trends) suggests considering the present Zr-containing ordered MAX phases as mechanically resilient candidates for conductive interlayers adjacent to bond-coat regions. Coating lifetime, however, is also governed by oxidation/TGO evolution and interfacial phase stability, which must be evaluated separately before application-specific conclusions are drawn.

3.3 Electronic properties

The electronic band structures in Fig. 4 show multiple bands crossing the Fermi level for both V_2ZrSiC_2 and Ti_2ZrSiC_2, confirming metallic character and the absence of an electronic band gap. Band crossings appear along both in-plane (Γ–M–K–Γ) and out-of-plane (Γ–A) directions, consistent with the layered MAX-phase framework in which charge transport is largely supported by the transition-metal sublattice, while covalent contributions arise from the stiff M–C network.

Table 3 Computed polycrystalline moduli B, G, and E (GPa), Poisson's ratio ν, Pugh ratio G/B, estimated Vickers hardness H_V (GPa), and directional Cauchy pressures P_a and P_c (GPa) for V_2ZrSiC_2 and Ti_2ZrSiC_2

Compounds		B	G	G/B	E	H_V	ν	P_a^{Cauchy}	P_c^{Cauchy}
V_2ZrSiC_2	This work	213.82	121.00	0.56	305.40	13.98	0.26	−47.84	−12.40
Ti_2ZrSiC_2	This work	187.88	135.79	0.72	328.29	21.19	0.20	−70.55	−41.52
V_2ScSnC_2	49	156.00	83.00	0.53	212.00	9.00	0.27	23.00	15.00
Zr_2TiSiC_2	26	183.00	133.00	0.73	321.00	21.00	0.20	−68.00	−44.00

Table 4 Elastic anisotropy factors (A_1, A_2, and A_3), linear compressibility ratio k_c/k_a, and auxiliary elastic-derived indicators: fracture toughness K_{IC} (MPa $m^{1/2}$), brittleness index M_B ($\mu m^{-1/2}$), acoustic impedance Z (Rayl), and radiation intensity I (m^4 kg^{-1} s^{-1}) for V_2ZrSiC_2 and Ti_2ZrSiC_2

Compounds	A_1	A_2	A_3	k_c/k_a	K_{IC}	M_B	$Z \times 10^6$	I
V_2ZrSiC_2	0.45	1.79	0.82	0.70	3.68	3.79	26.10	0.82
Ti_2ZrSiC_2	0.73	1.27	0.93	0.75	3.72	5.69	25.93	1.05

The TDOS/PDOS in Fig. 5 show that the states at and near E_F are dominated by transition-metal d orbitals: V-d and Zr-d for V_2ZrSiC_2, and Ti-d and Zr-d for Ti_2ZrSiC_2. Si-p and C-p states contribute primarily at lower energies in hybridized features below E_F, consistent with stronger covalent components in the M–C framework. The larger TDOS at E_F for V_2ZrSiC_2 indicates a higher electronic spectral weight at the Fermi level than that for Ti_2ZrSiC_2.

For quantitative reference, we estimate the Sommerfeld coefficient γ[64,65] and Pauli molar susceptibility χ_P[64,66] from the density of states at the Fermi level, $N(E_F)$. With $N(E_F)$ in states eV^{-1} f.u.$^{-1}$ (both spins), the electronic specific-heat coefficient is

$$\gamma = \frac{\pi^2 k_B^2}{3} N(E_F) N_A (1\ \text{eV})^{-1} \Rightarrow \gamma\left[\text{mJ mol}^{-1}\ \text{K}^{-2}\right] \approx 2.357 N(E_F), \quad (12)$$

and the Pauli susceptibility (reported in the common cgs laboratory convention) can be written as

$$\chi_P = \mu_0 \mu_B^2 N(E_F) N_A (1\ \text{eV})^{-1} \Rightarrow \chi_P[10^{-4}\ \text{emu mol}^{-1}] \approx 0.323 N(E_F), \quad (13)$$

where k_B is Boltzmann's constant, N_A Avogadro's number, μ_0 the vacuum permeability, and μ_B the Bohr magneton. The numerical prefactors in eqn (12) and (13) incorporate unit conversions (including SI-to-cgs conversion for susceptibility).[67] For the present non-magnetic calculations, the TDOS is written per spin, and we therefore convert to both spins as $N(E_F)_{both} = 2N(E_F)_{per\ spin}$. If a code reports DOS per unit cell, the DOS should additionally be divided by the number of formula units Z per cell; if the energy axis is in Rydberg, 1 Ry = 13.605693 eV.

Table 5 shows that V_2ZrSiC_2 has larger $N(E_F)$ and therefore larger γ and χ_P than Ti_2ZrSiC_2. A larger $N(E_F)$ implies a stronger electronic contribution to the low-temperature heat capacity and a larger Pauli (spin) susceptibility component for V_2ZrSiC_2 within the non-interacting DOS approximation. Conversely, the reduced $N(E_F)$ of Ti_2ZrSiC_2 indicates lower metallic spectral weight at E_F, consistent with its higher stiffness/hardness trends and more negative bonding indicators discussed in Section 3.2. Overall, the FP-LAPW+PBE electronic structures provide a consistent basis for comparing transport-relevant metallicity and Fermi-level descriptors in these ordered MAX phases, while environment-dependent oxidation and interface stability must be evaluated separately for coating-specific deployment.

3.4 Thermodynamic properties

3.4.1 Sound velocities, Debye temperature, and thermal-transport indicators. Using the VRH-averaged elastic moduli, the longitudinal, transverse, and average sound velocities[68] are

$$v_l = \sqrt{\frac{B + \frac{4}{3}G}{\rho}}, \quad v_t = \sqrt{\frac{G}{\rho}}, \quad v_m = \left[\frac{1}{3}\left(\frac{2}{v_t^3} + \frac{1}{v_l^3}\right)\right]^{-1/3}, \quad (14)$$

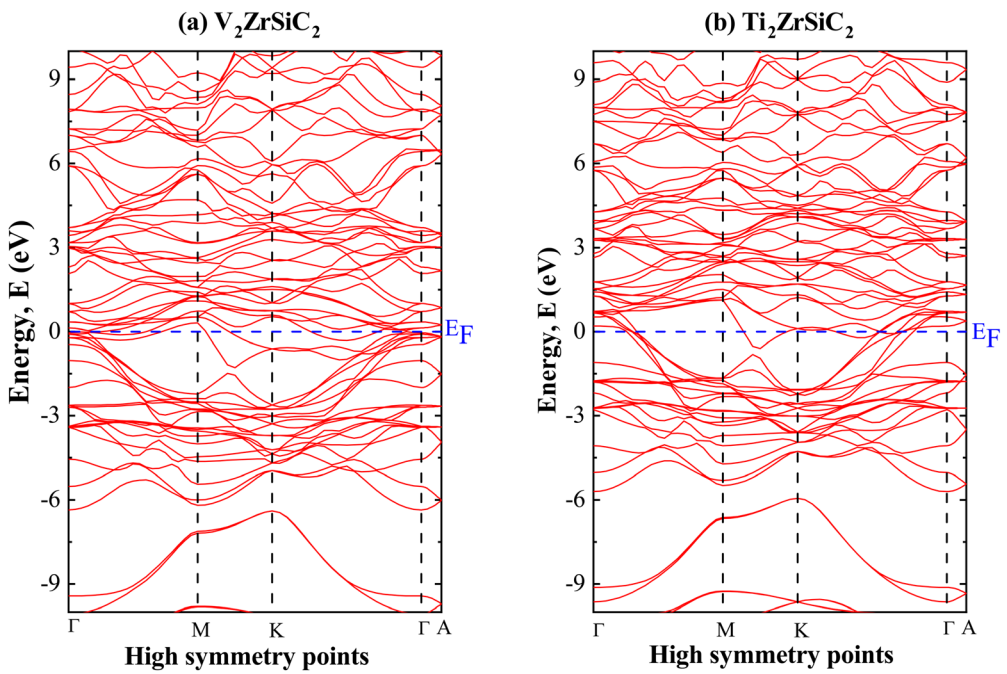

Fig. 4 Electronic band structures of (a) V_2ZrSiC_2 and (b) Ti_2ZrSiC_2 along the hexagonal high-symmetry path Γ–M–K–Γ–A.

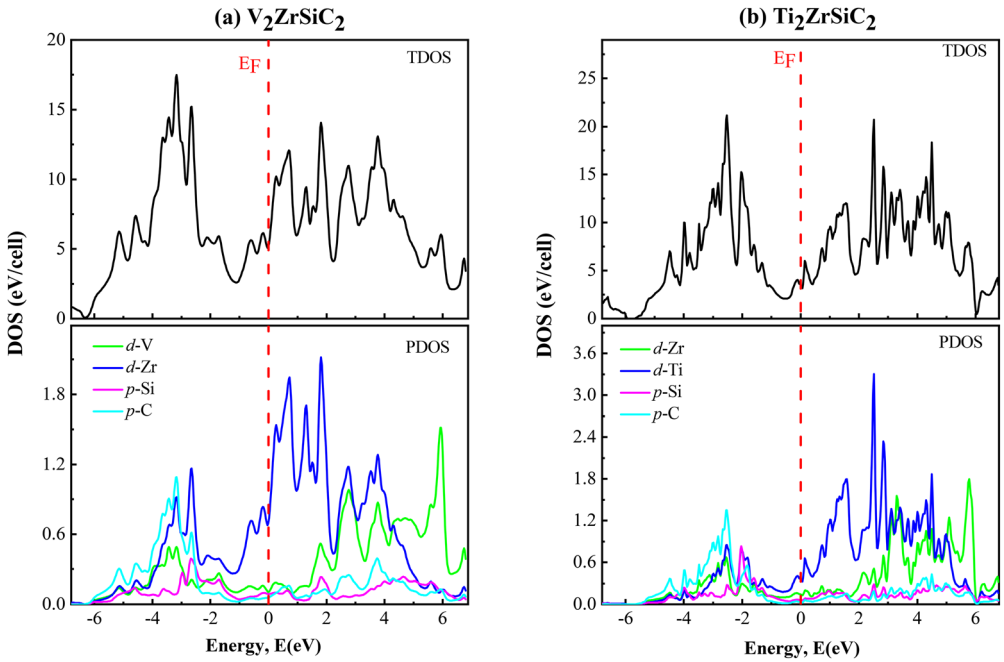

Fig. 5 Total density of states (TDOS, top) and atom/orbital-resolved partial DOS (bottom) for (a) V_2ZrSiC_2 and (b) Ti_2ZrSiC_2.

Table 5 Electronic metrics at the Fermi level after converting a per-spin TDOS to both spins: $N(E_F)_{both} = 2N(E_F)_{per\,spin}$. $N(E_F)$ is in states eV^{-1} f.u.$^{-1}$ (both spins). γ and χ_P are obtained from eqn (12) and (13)

Compound	$N(E_F)$ (both)	γ (mJ mol^{-1} K^{-2})	χ_P (10^{-4} emu mol^{-1})
V_2ZrSiC_2	5.3748	12.668	1.736
Ti_2ZrSiC_2	3.1616	7.452	1.021

where B and G are the Hill bulk and shear moduli (Pa), ρ is the mass density (kg m^{-3}), and v_l, v_t, and v_m are in m s^{-1}.

To capture pressure and temperature effects on thermoelastic response (*via V*), bulk modulus, heat capacity, and Debye temperature, we employ the semi-harmonic Debye model as implemented in Gibbs2.[48] Within this framework, the Debye temperature is written as[68]

$$\Theta_D = \frac{\hbar}{k_B}\left[6\pi^2 V^{1/2} r\right]^{1/3} f(\nu)\sqrt{\frac{B_s}{M}}, \quad (15)$$

where V and M are the molecular volume and molecular mass, r is the number of atoms per formula unit, B_s is the adiabatic bulk modulus (approximated here by the static bulk modulus), and $f(\nu)$ is a scaling function depending on Poisson's ratio ν:

$$f(\nu) = \left\{3\left[2\left(\frac{2}{3}\frac{1+\nu}{1-2\nu}\right)^{3/2} + \left(\frac{1}{3}\frac{1+\nu}{1-\nu}\right)^{3/2}\right]^{-1}\right\}^{1/3}. \quad (16)$$

The static (adiabatic) bulk modulus is obtained from the EOS curvature as

$$B_s \simeq B_{static} = V\left(\frac{d^2E(V)}{dV^2}\right). \quad (17)$$

As summarized in Table 6, Ti_2ZrSiC_2 has a lower density and higher sound velocities, leading to a larger Debye temperature (Θ_D = 726.05 K) than that for V_2ZrSiC_2 (Θ_D = 669.19 K). This ranking is consistent with the larger shear and Young's moduli of Ti_2ZrSiC_2 (Table 3), since v_t and thus v_m are governed primarily by shear rigidity through eqn (14). Relative to V_2ScSnC_2,[49] both Zr-containing phases show higher velocities and Θ_D, reflecting a stiffer elastic response; their Debye temperatures are comparable to that of Zr_2TiSiC_2.[26]

The melting temperature (T_m) is used here as a comparative indicator and is estimated using the semi-empirical relationship[74]

$$T_m = 354 + 1.5(2C_{11} + C_{13}), \quad (18)$$

which was fitted to a set of known crystals; accordingly, the values should be interpreted as comparative estimates rather than precise melting points. Table 6 indicates that Ti_2ZrSiC_2 has a slightly higher estimated T_m than V_2ZrSiC_2, consistent with its larger stiffness constants in Table 2.

For thermal transport, we report both a minimum (amorphous-limit) estimate and a crystalline (phonon) estimate. In the minimum-thermal-conductivity estimate, heat-carrying vibrational modes are assumed to have mean free paths limited to near-interatomic spacings.[75] A convenient expression is

$$k_{min} = \beta k_B n^{2/3}\left(\frac{N_A\rho}{M}\right)^{1/3} v_m, \quad (19)$$

where β is a dimensionless constant and $\beta \approx 0.87$, n is the number of atoms per formula unit, M is the molar mass, and v_m is from eqn (14).

Table 6 Computed density ρ (g cm^{-3}), sound velocities v_l, v_t, v_m (m s^{-1}), Debye temperature Θ_D (K), melting estimate T_m (K), minimum and lattice thermal conductivity at 300 K (k_{min} and k_{ph} in W m^{-1} K^{-1}), and thermal expansion coefficient at 300 K (α in $\times 10^{-5}$ K^{-1}) for V_2ZrSiC_2 and Ti_2ZrSiC_2

Compounds	Ref.	ρ	v_l	v_t	v_m	Θ_D	T_m	k_{min}	k_{ph}	α
V_2ZrSiC_2	This work	5.6334	8160.74	4634.68	5152.65	669.19	1862.98	1.03	9.99	2.42082
Ti_2ZrSiC_2	This work	4.9516	8631.93	5236.88	5786.91	726.05	1928.67	1.08	11.11	2.42767
V_2ScSnC_2	49	5.6195	6908.14	3855.40	4292.41	526.98	1533.32	0.48	68.94	—
Zr_2TiSiC_2	26	5.4951	8108.53	4923.28	5439.94	668.44	1891.66	0.61	81.85	—
Nb_2ScAlC_2	69	—	—	—	—	660.5	1842.6	1.256	46.03	—
Nb_2ScSiC_2	69	—	—	—	—	642.3	1863.0	1.251	34.49	—
Ti_2AlC	70	—	—	—	—	—	1548–1639	1.35	14.6 (1300 K)	—
Ti_2AlC	71	—	—	—	—	—	—	1.373	14.71(1300 K)	—
Ti_2AlC	Expt.[3]	—	—	—	—	—	—	—	16 (1300 K)	—
Al_2O_3	72	—	—	—	—	—	2323	—	—	—
$Y_4Al_2O_9$	73	—	—	—	—	564	—	1.12	—	—
Ti_3ZnC_2	11	—	—	—	—	617.9	1718.9	1.229	22.84	—
Ti_3GaC_2	11	—	—	—	—	702.1	1872.0	1.399	45.59	—
Ti_3GeC_2	11	—	—	—	—	707.0	1913.1	1.420	41.91	—
Ti_3AlC_2	11	—	—	—	—	780.7	1866.5	1.550	53.74	—
Ti_3SiC_2	11	—	—	—	—	806.4	1975.9	1.631	52.12	—
Ti_3InC_2	11	—	—	—	—	620.6	1782.2	1.208	36.31	—
Ti_3SnC_2	11	—	—	—	—	629.3	1808.8	1.230	36.24	—

Alternatively, Cahill's form is[75]

$$k_{min}^{Cahill} = \frac{\pi}{6^{1/3}} k_B n_a^{2/3} (v_l + 2v_t), \quad (20)$$

with atomic number density written inline as $n_a = N_A\rho/\bar{M} = nN_A\rho/M$ (where $\bar{M} = M/n$).

For crystalline phonon transport, a Slack-like model[51] is used, which yields an approximate $1/T$ behavior when Umklapp scattering dominates:

$$k_{ph}(T) = \frac{A\bar{M}\Theta_D{}^3\delta}{\gamma^2 n^{2/3} T}, \quad (21)$$

where $A(\gamma)$ is a dimensionless prefactor,

$$A(\gamma) = \frac{4.85628 \times 10^7}{2\left(1 - \frac{0.514}{\gamma} + \frac{0.228}{\gamma^2}\right)}. \quad (22)$$

Here $\bar{M} = M/n$ is the average atomic mass, δ is the cube root of the volume per atom, and γ is the Grüneisen parameter. To compute δ, we use $\delta = V_{atom}{}^{1/3}$, $V_{atom} = \frac{V_{cell}}{N}$ and the density–volume relation is $\rho = \frac{ZM}{N_A V_{cell}}$ with $Z = 2$ and $N = Zn = 12$ for the conventional 312 hexagonal cell. The Grüneisen parameter is defined as[76]

$$\gamma = -\frac{d \ln \Theta_D(V)}{d \ln V}. \quad (23)$$

At $T = 300$ K, the resulting Slack-like values are $k_{ph} = 9.99$ W m^{-1} K^{-1} for V_2ZrSiC_2 and 11.11 W m^{-1} K^{-1} for Ti_2ZrSiC_2 (Table 6). The lattice term decreases monotonically with T (Fig. 10), consistent with Umklapp-dominated thermal resistance and the explicit $1/T$ factor in eqn (21). Because Slack-type estimates depend sensitively on γ and volumetric descriptors, differences relative to ref. 26,49 should be interpreted primarily as model-based trends rather than absolute experimental benchmarks.

3.4.2 Quasi-harmonic temperature and pressure dependence of $V(T,P)$, $\Theta_D(T,P)$, $\alpha(T,P)$, and $C_V(T,P)$. Within the semi-harmonic Debye (Debye–Grüneisen) implementation used here,[65,77] the coupled pressure and temperature dependence of equilibrium volume and derived thermodynamic functions is obtained by minimizing the non-equilibrium Gibbs free energy

$$G^*(V,P,T) = E(V) + PV + A_{vib}(\Theta_D;T), \quad (24)$$

where $E(V)$ is the static 0 K DFT energy, PV is the hydrostatic pressure term at fixed V, and A_{vib} is the vibrational Helmholtz free energy[65,77]

$$A_{vib}(\Theta_D; T) = nk_B T\left[\frac{9\Theta_D}{8T} + 3\ln\left(1 - e^{-\Theta_D/T}\right) - D\left(\frac{\Theta_D}{T}\right)\right], \quad (25)$$

where $D(\Theta_D/T)$ denotes the Debye integral and n is the number of atoms per formula unit. The equilibrium curve $V(P,T)$ is obtained from

$$\left[\frac{\partial G^*(V,P,T)}{\partial V}\right]_{P,T} = 0, \quad (26)$$

and the isothermal bulk modulus B_T, isochoric heat capacity C_V, and thermal expansion coefficient α follow as[65,77]

$$B_T(P,T) = V\left[\frac{\partial^2 G^*(V,P,T)}{\partial V^2}\right]_{P,T}, \quad (27)$$

$$C_V = 3nk_B\left[4D\left(\frac{\Theta_D}{T}\right) - \frac{\left(\frac{3\Theta_D}{T}\right)}{e^{\Theta_D/T} - 1}\right], \quad (28)$$

$$\alpha = \frac{\gamma C_V}{B_T V}, \quad (29)$$

where γ is the Grüneisen parameter defined in eqn (23). These relations rationalize the principal pressure trends:

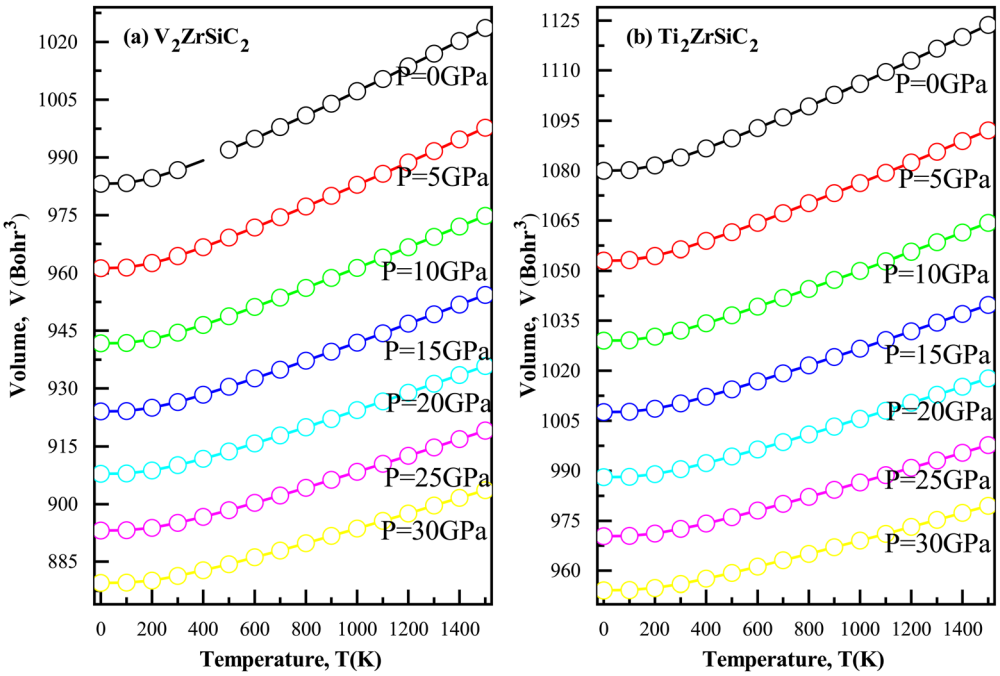

Fig. 6 Temperature dependence of the unit-cell volume $V(T)$ at pressures P = 0–30 GPa for (a) V_2ZrSiC_2 and (b) Ti_2ZrSiC_2 within the quasi-harmonic Debye–Grüneisen model.

compression increases B_T and decreases V, while also increasing $\Theta_D(V)$, which together reduce α and slightly suppress C_V at fixed T.

The equilibrium volumes obtained from eqn (26) are shown in Fig. 6. In both compounds, $V(T)$ increases with temperature at all pressures due to vibrational expansion, while increasing pressure shifts the curves to lower volumes and reduces the temperature slope.

The Debye temperatures in Fig. 7 decrease gradually with increasing temperature but increase markedly with pressure. Within the Debye–Grüneisen picture, the pressure enhancement follows from eqn (23): compression reduces V and

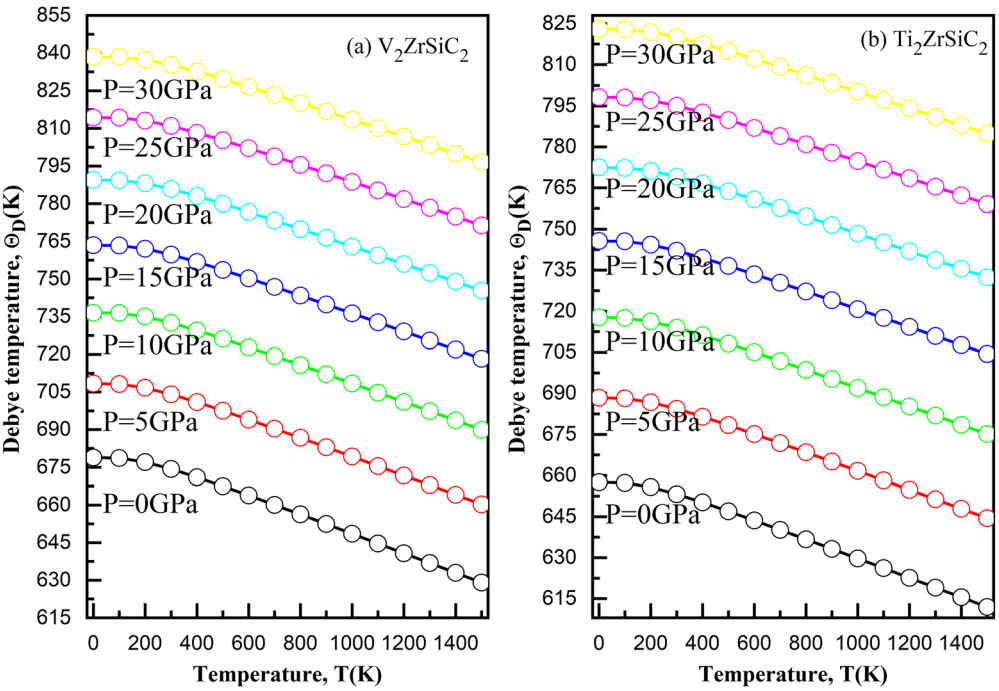

Fig. 7 Debye temperature $\Theta_D(T)$ at pressures P = 0–30 GPa for (a) V_2ZrSiC_2 and (b) Ti_2ZrSiC_2 within the Debye–Grüneisen model.

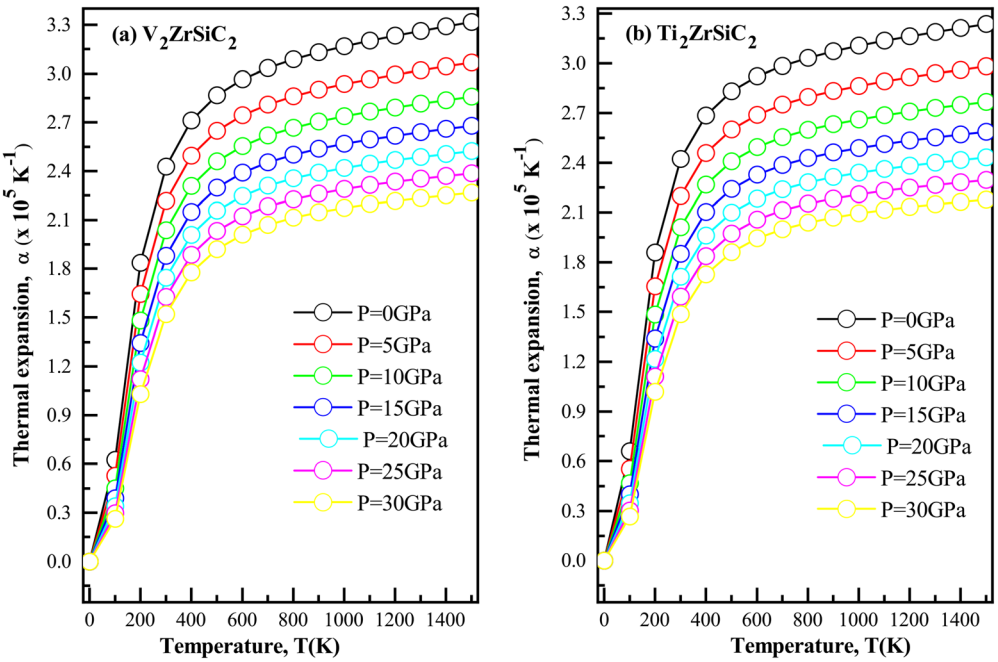

Fig. 8 Thermal expansion coefficient $\alpha(T)$ at pressures P = 0–30 GPa for (a) V_2ZrSiC_2 and (b) Ti_2ZrSiC_2 within the Debye–Grüneisen model.

increases Θ_D, consistent with lattice stiffening. Across the full (T,P) window, Ti_2ZrSiC_2 maintains a higher Θ_D than V_2ZrSiC_2, consistent with its higher v_m values in Table 6.

The thermal expansion coefficient in Fig. 8 rises rapidly at low temperature and approaches a smoother high-temperature regime, while increasing pressure systematically reduces $\alpha(T)$ for both compounds. Eqn (29) makes explicit why α is suppressed under pressure: B_T increases and V decreases, reducing α at fixed C_V and γ.

The isochoric heat capacity curves in Fig. 9 follow the expected Debye behavior.[65,77] At low temperature they increase rapidly with T, while at high temperature they approach the classical Dulong–Petit limit, $C_V \rightarrow 3nR$ per mole of formula units.[65,78]

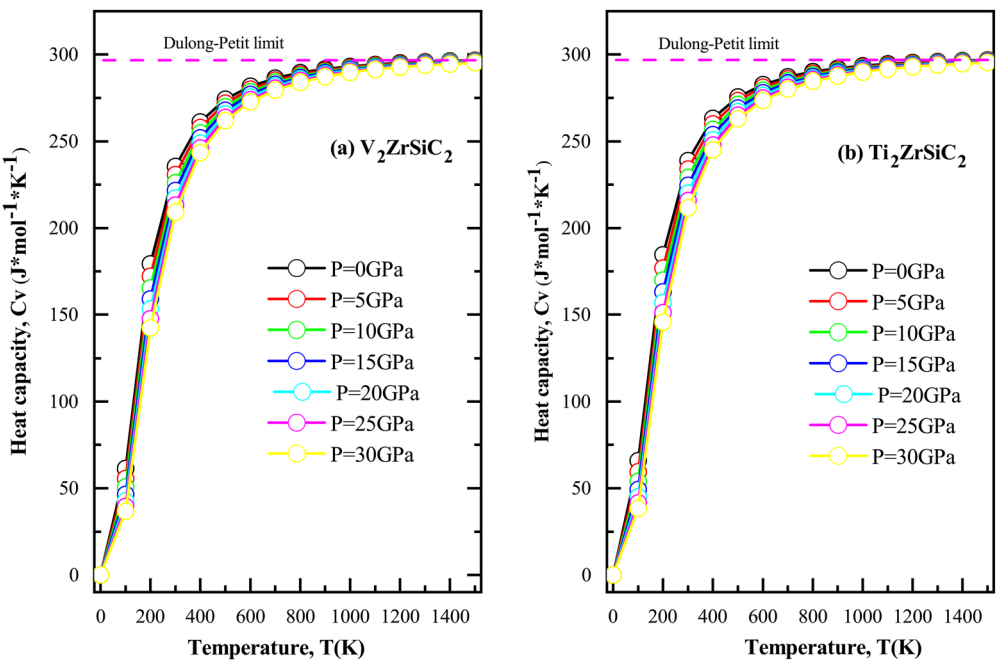

Fig. 9 Isochoric heat capacity $C_V(T)$ at pressures P = 0–30 GPa for (a) V_2ZrSiC_2 and (b) Ti_2ZrSiC_2.

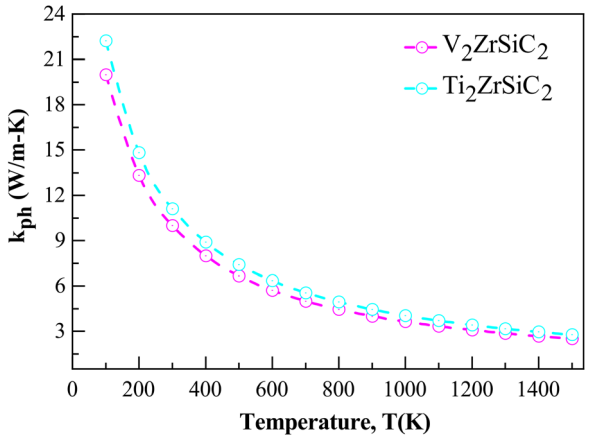

Fig. 10 Predicted lattice thermal conductivity $k_{ph}(T)$ for V_2ZrSiC_2 and Ti_2ZrSiC_2 from the Slack-like model.

Fig. 10 summarizes the predicted lattice thermal conductivity $k_{ph}(T)$ for V_2ZrSiC_2 and Ti_2ZrSiC_2. The higher k_{ph} of Ti_2ZrSiC_2 across the temperature window is consistent with its higher Θ_D and sound velocities, while the overall decay with temperature is consistent with the approximate $1/T$ scaling expected for Umklapp-dominated phonon scattering in Slack-like models.[51,75]

To visualize the corresponding free-energy trends, Fig. 11 presents the Gibbs free energy $G(T,P)$ and vibrational free energy $F_{vib}(T,P)$ obtained within the same Debye–Grüneisen framework.

Here, $F_{vib}(T,P)$ represents the vibrational Helmholtz contribution (eqn (25)) up to the chosen reference. For both compounds, G decreases with increasing temperature at all pressures due to the increasing vibrational contribution, while increasing pressure shifts G through the PV term and the pressure-driven reduction in equilibrium volume. The vibrational free energy becomes increasingly negative with temperature, and its pressure dependence reflects the pressure-enhanced Debye temperature and reduced vibrational entropy under compression. These free-energy trends provide a finite-temperature thermodynamic baseline within the present quasi-harmonic Debye treatment and complement the $V(T,P)$, $\Theta_D(T,P)$, $\alpha(T,P)$, and $C_V(T,P)$ responses reported above.

Overall, both ordered MAX phases exhibit high vibrational stiffness (high Θ_D), a pressure-suppressed thermal expansion response, and a decreasing $k_{ph}(T)$ trend with temperature. In the context of coating architectures, these thermoelastic and transport indicators position V_2ZrSiC_2 and Ti_2ZrSiC_2 as screening-level candidates for conductive, mechanically resilient layers rather than stand-alone insulating TBC top coats, while emphasizing that oxidation resistance and interfacial phase stability must be evaluated separately for application-specific conclusions.

3.5 Implications for TBC architectures

Thermal-barrier coating (TBC) systems are typically designed as a multilayer stack consisting of a ceramic top coat (most commonly YSZ), a thermally grown oxide (TGO; often α-Al_2O_3 in alumina-forming systems), and an oxidation-resistant bond

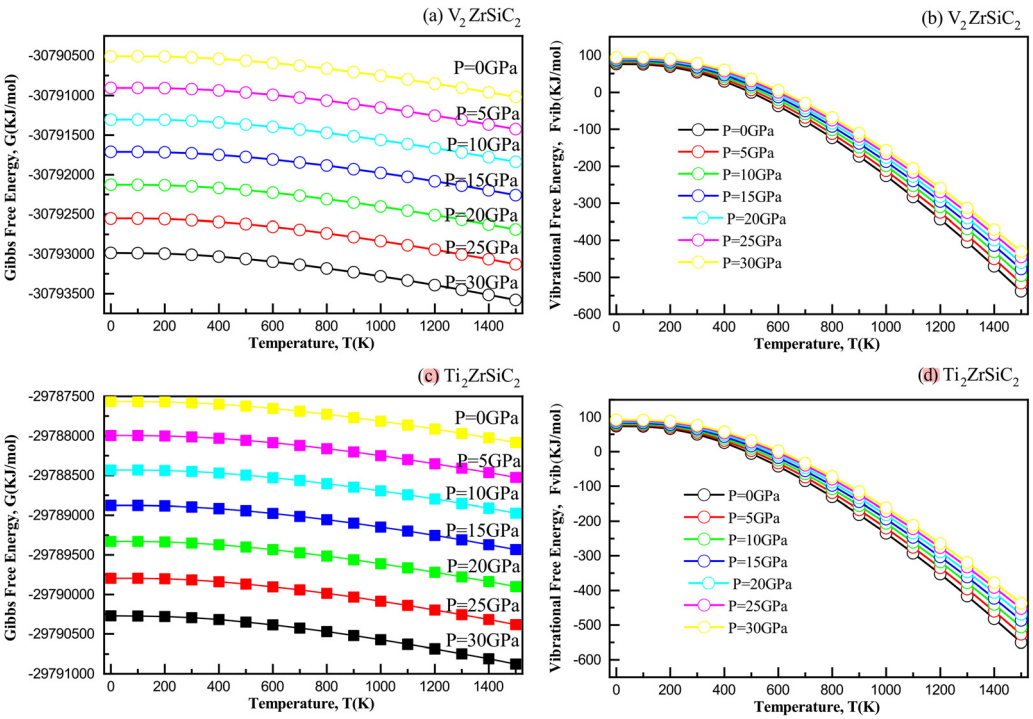

Fig. 11 Finite-temperature free-energy trends from the quasi-harmonic Debye–Grüneisen model. (a) Gibbs free energy $G(T)$ for V_2ZrSiC_2, (b) vibrational free energy $F_{vib}(T)$ for V_2ZrSiC_2, (c) $G(T)$ for Ti_2ZrSiC_2 and (d) $F_{vib}(T)$ for Ti_2ZrSiC_2.

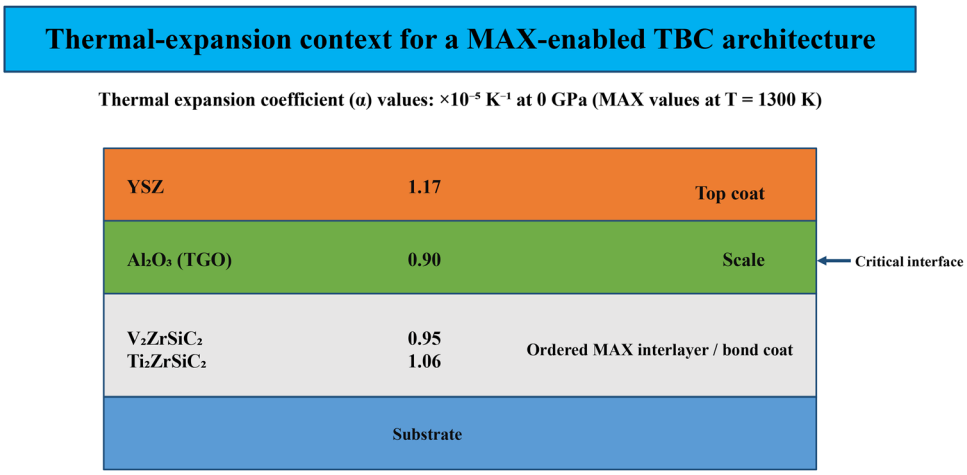

Fig. 12 Thermal-expansion context for a MAX-enabled TBC architecture (YSZ top coat/α-Al_2O_3 TGO/ordered MAX interlayer/substrate). Values are shown as linear CTE in units of 10^{-5} K^{-1} at 0 GPa (MAX values evaluated at T = 1300 K).

coat/interlayer on a high-temperature structural substrate.[79] In such stacks, thermal-expansion mismatch during heating/cooling generates cyclic stresses that concentrate at interfaces, especially near the TGO/interlayer region, and can trigger cracking and spallation.[80] Consequently, a key selection requirement for any candidate interlayer/bond-coat-adjacent layer is compatibility of the linear coefficient of thermal expansion (CTE) with both the TGO and top coat, together with sufficient mechanical integrity at temperature and acceptable oxidation/interfacial reactivity.[81]

A useful benchmark comes from high-temperature durability studies of YSZ deposited on alumina-forming MAX substrates, where improved CTE compatibility among YSZ, α-Al_2O_3, and the MAX layer was identified as a contributor to delayed failure and tolerance of comparatively thicker TGOs under stepped furnace exposure up to 1300 °C.[16] Representative linear CTE values reported in ref. 16 include YSZ ($\sim 11.7 \times 10^{-6}$ K^{-1}), α-Al_2O_3 ($\sim 9 \times 10^{-6}$ K^{-1}), and Ti_2AlC ($\sim 10.2 \times 10^{-6}$ K^{-1}), illustrating why alumina-forming MAX layers can reduce mismatch at the critical interface compared with higher-CTE metallic substrates.

In the present work, the quasi-harmonic Debye–Grüneisen treatment yields the volumetric thermal expansion coefficient $\alpha_V(T)$ through eqn (29). To compare directly with conventional linear CTE values used in TBC design, we use the isotropic relation $\alpha_L(T) \approx \alpha_V(T)/3$. Fig. 12 places the resulting α_L values for V_2ZrSiC_2 and Ti_2ZrSiC_2 evaluated at T = 1300 K and P = 0 alongside representative YSZ and α-Al_2O_3 values. The ordered MAX phases fall between the TGO and top-coat values (V_2ZrSiC_2: 0.95×10^{-5} K^{-1}; Ti_2ZrSiC_2: 1.06×10^{-5} K^{-1} at 1300 K), compared with YSZ (1.17×10^{-5} K^{-1}) and α-Al_2O_3 (0.90×10^{-5} K^{-1}). If the substrate has a substantially higher CTE than the MAX interlayer, graded or intermediate designs may be required to minimize stress concentrations during thermal cycling.

The CTE comparison in Fig. 12 provides only one necessary compatibility criterion for TBC interlayers. Practical TBC lifetime is frequently dominated by oxidation kinetics, TGO growth stresses, and interfacial phase equilibria/reaction products with YSZ and alumina. These chemistry- and environment-specific factors are not explicitly modeled here (*e.g.*, no oxidation thermodynamics, no interface reaction modeling, and no competing-phase stability analysis at finite temperature beyond the present Debye–Grüneisen free-energy trends). Accordingly, the present results position V_2ZrSiC_2 and Ti_2ZrSiC_2 as screening-level candidates for further evaluation as conductive, thermally compatible layers in coating architectures, while emphasizing that oxidation behavior, particularly for V- and Si-containing compositions, and interface stability must be established through dedicated thermodynamic calculations and experiments before application-specific conclusions can be drawn.

4 Conclusion

First-principles FP-LAPW calculations within GGA-PBE were employed to investigate the chemically ordered quaternary MAX phases V_2ZrSiC_2 and Ti_2ZrSiC_2 in both α- and β-stacking variants. Equation-of-state fitting reveals pronounced stacking sensitivity in volumetric rigidity: the α polytypes are significantly stiffer, with bulk moduli of ~216 GPa (V_2ZrSiC_2) and ~192 GPa (Ti_2ZrSiC_2), whereas the corresponding β polytypes are more compressible (~178 GPa and ~157 GPa). All computed elastic constants satisfy the Born stability criteria for hexagonal crystals. Voigt–Reuss–Hill averages indicate that Ti_2ZrSiC_2 provides higher shear/tensile rigidity ($G \approx 136$ GPa and $E \approx 328$ GPa) together with a higher hardness estimate ($H_V \approx 21$ GPa), while V_2ZrSiC_2 retains the higher bulk modulus ($B \approx 214$ GPa), *i.e.*, greater incompressibility. Harmonic phonon dispersions exhibit no imaginary frequencies, suggesting dynamical stability of the optimized structures.

Both compounds are metallic, with transition-metal d states dominating near the Fermi level; V_2ZrSiC_2 exhibits the larger $N(E_F)$ and therefore larger electronic spectral weight at E_F.

Within the quasi-harmonic Debye–Grüneisen framework, the computed thermodynamic trends ($V(T,P)$, $\Theta_D(T,P)$, $\alpha(T,P)$, and $C_V(T,P)$) together with the reported Gibbs and vibrational free-energy curves provide a finite-temperature baseline for the assumed MAX-phase structures. Debye temperatures of ~669 K (V_2ZrSiC_2) and ~726 K (Ti_2ZrSiC_2), and semi-empirical melting estimates near 1863 K and 1929 K, further support comparative screening of high-temperature robustness.

Competing-phase stability was further assessed using the energy above the convex hull, ΔE_{hull} (Table 1). The nonzero ΔE_{hull} values (~0.10–0.19 eV per atom across the investigated stackings) indicate metastability at T = 0 K with respect to competing phases within the adopted phase set. Accordingly, the present results are best interpreted as a first-principles property screen for ordered MAX prototypes; a definitive synthesizability assessment would require a comprehensive competing-phase analysis (and, ideally, finite-temperature competing-phase free energies).

From an application viewpoint, these Zr-containing ordered MAX phases are not intended as insulating TBC top coats; rather, their combination of stiffness, metallic conduction, and thermoelastic response motivates consideration as conductive, mechanically resilient layers within coating architectures. The computed linear CTE values at 1300 K ($\alpha_L \approx 0.95 \times 10^{-5}$ K^{-1} for V_2ZrSiC_2 and $\alpha_L \approx 1.06 \times 10^{-5}$ K^{-1} for Ti_2ZrSiC_2) fall between representative α-Al_2O_3 ($\sim 0.90 \times 10^{-5}$ K^{-1}) and YSZ ($\sim 1.17 \times 10^{-5}$ K^{-1}) values, indicating CTE-level compatibility at the TGO/top-coat side of the stack. At the same time, practical TBC performance is controlled by oxidation/TGO evolution and interfacial phase equilibria; these chemistry-specific factors are not explicitly modeled here and must be assessed separately before application-specific conclusions can be drawn. Overall, the present dataset identifies Ti_2ZrSiC_2 as the more attractive option for load-bearing and wear-related roles (higher G, E, and H_V), while V_2ZrSiC_2 offers higher incompressibility and larger electronic spectral weight at the Fermi level, motivating further targeted thermodynamic analysis and experimental investigation.

Conflicts of interest

There are no conflicts to declare.

Data availability

All data supporting the findings of this study are contained within this article. Additional data, including raw and processed computational outputs, are available from the corresponding author upon reasonable request.

References

1 M. W. Barsoum, The $M_{N+1}AX_N$ phases: A new class of solids, *Prog. Solid State Chem.*, 2000, **28**, 201–281, DOI: 10.1016/S0079-6786(00)00006-6.
2 M. Sokol, V. Natu, S. Kota and M. W. Barsoum, On the chemical diversity of the MAX phases, *Trends Chem.*, 2019, **1**, 210–223, DOI: 10.1016/j.trechm.2019.02.016.
3 M. W. Barsoum, *MAX phases: properties of machinable ternary carbides and nitrides*, Wiley, Weinheim, 1st edn, 2013, https://onlinelibrary.wiley.com/doi/book/10.1002/9783527654581.
4 W. Jeitschko, H. Nowotny and F. Benesovsky, Carbides of formula T_2MC, *J. Less-Common Met.*, 1964, **7**, 133–138, DOI: 10.1016/0022-5088(64)90055-4.
5 J. Wang and Y. Zhou, Recent progress in theoretical prediction, preparation, and characterization of layered ternary transition-metal carbides, *Annu. Rev. Mater. Res.*, 2009, **39**, 415–443, DOI: 10.1146/annurev-matsci-082908-145340.
6 M. W. Barsoum and M. Radovic, Elastic and mechanical properties of the MAX phases, *Annu. Rev. Mater. Res.*, 2011, **41**, 195–227, DOI: 10.1146/annurev-matsci-062910-100448.
7 X. H. Wang and Y. C. Zhou, Layered machinable and electrically conductive Ti_2AlC and Ti_3AlC_2 ceramics: a review, *J. Mater. Sci. Technol.*, 2010, **26**, 385–416, DOI: 10.1016/S1005-0302(10)60064-3.
8 M. N. Amin, A. Al Faysal, A. Azzouz-Rached, F. I. Chowdhury, J. Uddin, J. Uddin, J. Islam, A. R. Piyal, A. K. Chowdhury and A. K. M. Rahman, DFT insights into the structural, mechanical, electronic, optical, and thermal properties of Cr_2AC (A = Si, Al, Ga, Ge, and P) MAX phases carbides, *AIP Adv.*, 2024, **14**, 125302, DOI: 10.1063/5.0234895.
9 A. Bouhemadou, Calculated structural, electronic and elastic properties of M_2GeC (M = Ti, V, Cr, Zr, Nb, Mo, Hf, Ta and W), *Appl. Phys. A: Mater. Sci. Process.*, 2009, **96**, 959–967, DOI: 10.1007/s00339-009-5106-5.
10 M. A. Ali, M. M. Hossain, M. A. Hossain, M. T. Nasir, M. M. Uddin, M. Z. Hasan, A. K. M. A. Islam and S. H. Naqib, Recently synthesized $(Zr_{1-x}Ti_x)_2AlC$ ($0 \leq x \leq 1$) solid solutions: theoretical study of the effects of M mixing on physical properties, *J. Alloys Compd.*, 2018, **743**, 146–154, DOI: 10.1016/j.jallcom.2018.01.396.
11 M. A. Hadi, I. Ahmed, M. A. Ali, M. M. Hossain, M. T. Nasir, M. L. Ali, S. H. Naqib and A. K. M. A. Islam, A comparative DFT exploration on M- and A-site double transition metal MAX phase Ti_3ZnC_2, *Open Ceram.*, 2022, **12**, 100308, DOI: 10.1016/j.oceram.2022.100308.
12 M. Roknuzzaman, M. A. Hadi, M. A. Ali, M. M. Hossain, N. Jahan, M. M. Uddin, J. A. Alarco and K. Ostrikov, First hafnium-based MAX phase in the 312 family, Hf_3AlC_2: a first-principles study, *J. Alloys Compd.*, 2017, **727**, 616–626, DOI: 10.1016/j.jallcom.2017.08.151.
13 M. R. H. Niloy, M. M. A. Alwi, M. D. N. Amin and A. N. Butt, Density functional theory study of pressure-induced structural, mechanical, electronic, optical, and thermal properties of Mo_2AC (A = Al, Ga, Ge), *J. Am. Ceram. Soc.*, 2026, **109**, e70298, DOI: 10.1111/jace.70298.
14 M. Naguib, V. N. Mochalin, M. W. Barsoum and Y. Gogotsi, 25th anniversary article: MXenes: a new family of two-dimensional materials, *Adv. Mater.*, 2014, **26**, 992–1005, DOI: 10.1002/adma.201304138.

15 X. Lei and N. Lin, Structure and synthesis of MAX phase materials: a brief review, *Crit. Rev. Solid State Mater. Sci.*, 2022, **47**, 736–771, DOI: 10.1080/10408436.2021.1966384.
16 J. L. Smialek, B. J. Harder and A. Garg, *Extreme Oxidative Durability of TBCs on Ti_2AlC MAX Phases,* Materials Science and Technology (MS&T), Columbus, OH, 2015 (NASA Glenn Research Center).
17 R. Meshkian, Q. Tao, M. Dahlqvist, J. Lu, L. Hultman and J. Rosen, Theoretical stability and materials synthesis of a chemically ordered MAX phase, Mo_2ScAlC_2, and its two-dimensional derivate Mo_2ScC_2 MXene, *Acta Mater.*, 2017, **125**, 476–480, DOI: 10.1016/j.actamat.2016.12.008.
18 P. A. Burr, D. Horlait and W. E. Lee, Experimental and DFT investigation of $(Cr,Ti)_3AlC_2$ MAX phase stability, *Mater. Res. Lett.*, 2017, **5**, 144–157, DOI: 10.1080/21663831.2016.1222598.
19 Z. Liu, E. Wu, J. Wang, Y. Qian, H. Xiang, X. Li, Q. Jin, G. Sun, X. Chen, J. Wang and M. Li, Crystal structure and formation mechanism of $(Cr_{2/3}Ti_{1/3})_3AlC_2$ MAX phase, *Acta Mater.*, 2014, **73**, 186–193, DOI: 10.1016/j.actamat.2014.04.006.
20 P. Xiao, N. Jin and Z. Lin, Double transition metal-containing M_2TiAlC_2 o-MAX phases as Li-ion battery anodes: a theoretical screening, *Mater. Res. Lett.*, 2021, **9**, 516–522, DOI: 10.1080/21663831.2021.1984997.
21 A. Azzouz-Rached, M. Traiche, A. Bouhenna, N. Rahman, M. Husain, A. Bentouaf, A. H. Alfaifi, W. M. Almalki, H. Albalawi, K. M. Abualnaja, E. Almutib, H. Rekab-Djabri and M. Fellah, DFT insights into double transition metal $M_2M'SiC_2$ MAX phases: prospects as thermal barrier coatings, *Case Stud. Therm. Eng.*, 2025, **72**, 106334, DOI: 10.1016/j.csite.2025.106334.
22 M. N. Amin, A. Azzouz-Rached, A. Chowdhury, M. R. H. Niloy, M. S. Khan, A. K. Chowdhury, A. K. M. Rahman, E. Hoq, M. S. Hoq and Y. Meddahi, DFT study of selected double transition metal MAX phases $M_2M'AC_2$ for thermal barrier coatings, *Adv. Theory Simul.*, 2025, e01443, DOI: 10.1002/adts.202501443.
23 E. Zapata-Solvas, S. G. Christopoulos, N. Ni, D. C. Parfitt, D. Horlait, M. E. Fitzpatrick, A. Chroneos and W. E. Lee, Experimental synthesis and density functional theory investigation of radiation tolerance of $Zr_3(Al_{1-x}Si_x)C_2$ MAX phases, *J. Am. Ceram. Soc.*, 2017, **100**, 1377–1387, DOI: 10.1111/jace.14742.
24 D. Bowden, J. Ward, S. Middleburgh, S. De Moraes Shubeita, E. Zapata-Solvas, T. Lapauw, J. Vleugels, K. Lambrinou, W. E. Lee, M. Preuss and P. Frankel, Stability of irradiation-induced defects in Zr_3AlC_2, Nb_4AlC_3 and $(Zr_{0.5},Ti_{0.5})_3AlC_2$ MAX phase-based ceramics, *Acta Mater.*, 2020, **183**, 24–35, DOI: 10.1016/j.actamat.2019.10.049.
25 A. A. Belkacem, H. Rached, M. Caid, Y. Rached, D. Rached, N. T. Mahmoud and N. Benkhettou, Stability analysis and efficiency of the new MAX-phase compounds M_3GaC_2 (M = Ti or Zr): a first-principles assessment, *Results Phys.*, 2022, **38**, 105621, DOI: 10.1016/j.rinp.2022.105621.
26 D. Behera, A. Dixit, A. Azzouz-Rached, A. Bentouaf, M. Ferdous Rahman, H. Albalawi, A. Bouhenna, E. S. Yousef and R. Sharma, Prediction of new MAX phase Zr_2MSiC_2 (M = Ti, V) compounds as a promising candidate for future engineering: DFT calculations, *Mater. Sci. Eng. B*, 2024, **301**, 117141, DOI: 10.1016/j.mseb.2023.117141.
27 R. Khatun, A. Rahman, D. C. Roy, A. A. Khatun, M. Hossain, U. Rani, P. K. Kamlesh, A. Irfan and S. C. Mouna, DFT study on the structural, mechanical, electronic, optical and thermodynamic properties of recently synthesized MAX phase compounds A_3InC_2 (A = Zr, Hf) under ambient and elevated pressure, *Mater. Today Commun.*, 2024, **40**, 109964, DOI: 10.1016/j.mtcomm.2024.109964.
28 A. Azzouz-Rached, M. M. Haque Babu, H. Rached, T. Hadji and D. Rached, Prediction of new Sn-based MAX phases for nuclear industry applications: DFT calculations, *Mater. Today Commun.*, 2021, **27**, 102233, DOI: 10.1016/j.mtcomm.2021.102233.
29 G. Surucu, Investigation of structural, electronic, anisotropic elastic, and lattice dynamical properties of MAX phase borides: an ab-initio study on hypothetical M_2AB (M = Ti, Zr, Hf; A = Al, Ga, In) compounds, *Mater. Chem. Phys.*, 2018, **203**, 106–117, DOI: 10.1016/j.matchemphys.2017.09.050.
30 M. A. Ali, M. M. Hossain, M. M. Uddin, A. Islam, D. Jana and S. Naqib, DFT insights into new B-containing 212 MAX phases Hf_2AB_2 (A = In, Sn), *J. Alloys Compd.*, 2021, **860**, 158408, DOI: 10.1016/j.jallcom.2020.158408.
31 M. M. A. Alwi and M. D. N. Amin, Magnetism-controlled mechanical and thermal properties of orthorhombic layered M_2AB_2 (M = Fe, Mn, V; A = Al, Ga): Implications for reduced lattice heat transport, *Surf. Interfaces*, 2026, **87**, 108878, DOI: 10.1016/j.surfin.2026.108878.
32 N. Espallargas, J. Berget, J. M. Guilemany, A. V. Benedetti and P. H. Suegama, Cr_3C_2-NiCr and WC-Ni thermal spray coatings as alternatives to hard chromium for erosion-corrosion resistance, *Surf. Coat. Technol.*, 2008, **202**, 1405–1417, DOI: 10.1016/j.surfcoat.2007.06.048.
33 M. Honglin, Z. Haichao, T. Honggang, M. Guozheng, L. Ming, W. Haidou, X. Fengkuan and C. Zhihai, Effects of hBN content and particle size on microstructure, mechanical and tribological properties of NiCr-Cr_3C_2-hBN coatings, *Surf. Coat. Technol.*, 2024, **478**, 130330, DOI: 10.1016/j.surfcoat.2023.130330.
34 C. Magnus, J. Sharp and W. M. Rainforth, Lubricating properties of spark plasma sintered (SPS) Ti_3SiC_2 MAX phase compound and composite, *Tribol. Trans.*, 2020, **63**, 38–51, DOI: 10.1080/10402004.2019.1657534.
35 M. A. Ali, M. M. Hossain, N. Jahan, A. K. M. A. Islam and S. H. Naqib, Newly synthesized Zr_2AlC, $Zr_2(Al_{0.58}Bi_{0.42})C$, $Zr_2(Al_{0.2}Sn_{0.8})C$, and $Zr_2(Al_{0.3}Sb_{0.7})C$ MAX phases: a DFT-based first-principles study, *Comput. Mater. Sci.*, 2017, **131**, 139–145, DOI: 10.1016/j.commatsci.2017.01.048.
36 J. Sun, Z. Zhang, Y. Zhang, X. Zhang, J. Guo, Q. Fu and L. Wu, High-temperature ablation resistance prediction of ceramic coatings using machine learning, *J. Am. Ceram. Soc.*, 2025, **108**, e20136, DOI: 10.1111/jace.20136.
37 K. Xu, X. Xiao, L. Wang, M. Lou, F. Wang, C. Li, H. Ren, X. Wang and K. Chang, Data-driven materials research and

development for functional coatings, *Adv. Sci.*, 2024, **11**, 2405262, DOI: 10.1002/advs.202405262.

38 H. Zhang, T. Hu, X. Wang and Y. Zhou, Structural defects in MAX phases and their derivative MXenes: a look forward, *J. Mater. Sci. Technol.*, 2020, **38**, 205–220, DOI: 10.1016/j.jmst.2019.03.049.

39 A. Azzouz-Rached, M. D. N. Amin, H. Merkoune, I. Ouadha, A. Shtaiwi and A. M. Al-Zuheiri, *et al.*, Structural, thermo-mechanical, and transport properties of Ti_2NbSiC_2 and Ti_2MoSiC_2 MAX phases as candidates for high-temperature structural and coating materials, *J. Am. Ceram. Soc.*, 2026, **109**, e70502, DOI: 10.1111/jace.70502.

40 P. Blaha, K. Schwarz, P. Sorantin and S. B. Trickey, Full-potential, linearized augmented plane wave programs for crystalline systems, *Comput. Phys. Commun.*, 1990, **59**, 399–415, DOI: 10.1016/0010-4655(90)90187-6.

41 A. Bouhenna, A. Azzouz-Rached, W. M. Almalki, O. Zeggai, N. Sfina, N. Rahman, M. Husain, M. Fellah, Y. M. Alawaideh and M. Uzair, First-principles calculations to investigate physical properties of oxide perovskites $LaBO_3$ (B = Mn, Fe) for thermo-spintronic devices, *J. Phys. Chem. Solids*, 2025, **196**, 112362, DOI: 10.1016/j.jpcs.2024.112362.

42 P. Blaha, K. Schwarz, G. K. H. Madsen, D. Kvasnicka, J. Luitz, R. Laskowski, F. Tran, L. Marks and L. Marks, *WIEN2k: an augmented plane wave plus local orbitals program for calculating crystal properties*, Vienna University of Technology, 2001.

43 N. Rahman, M. Husain, W. Ullah, A. Azzouz-Rached, H. Albalawi, Z. Bayhan and S. A. Alsalhi, Comprehensive analysis of structural, mechanical, optoelectronic, and thermodynamic properties of Ba_2XBiO_6 (X = Y, La) double perovskites using density functional theory, *Phys. Scr.*, 2024, **99**, 095984, DOI: 10.1088/1402-4896/ad6e30.

44 N. Rahman, M. Husain, W. Ullah, A. Azzouz-Rached, N. Algethami, B. M. Al-Khamiseh, K. M. Abualnaja, G. Alosaimi, H. Albalawi, Z. Bayhan and S. A. Alsalhi, Exploring the structural, elastic and optoelectronic properties of stable Sr_2XSbO_6 (X = Dy, La) double perovskites: ab initio calculations, *J. Inorg. Organomet. Polym. Mater.*, 2024, **34**, 5102–5112, DOI: 10.1007/s10904-024-03194-1.

45 J. P. Perdew, K. Burke and M. Ernzerhof, Generalized gradient approximation made simple, *Phys. Rev. Lett.*, 1996, **77**, 3865–3868, DOI: 10.1103/PhysRevLett.77.3865.

46 M. Jamal, IRelast. A package for calculating elastic tensors. Available from: https://www.wien2k.at/ (2018).

47 W. Frank, C. Elsässer and M. Fähnle, Ab initio Force-Constant Method for Phonon Dispersions in Alkali Metals, *Phys. Rev. Lett.*, 1995, **74**, 1791–1794, DOI: 10.1103/PhysRevLett.74.1791.

48 A. Otero-de-la-Roza, D. Abbasi-Pérez and V. Luaña, Gibbs2: a new version of the quasiharmonic model code. II. Models for solid-state thermodynamics, features and implementation, *Comput. Phys. Commun.*, 2011, **182**, 2232–2248, DOI: 10.1016/j.cpc.2011.05.009.

49 A. Azzouz-Rached, M. Azzouz-Rached, N. Rahman, M. Husain, N. Sfina, V. Tirth, A. Bentouaf, M. Ferdous Rahman, N. Algethami, H. A. Althobaiti, K. M. Abualnaja and G. Alosaimi, Exploring highly energetic quaternary double transition metal MAX phase M_2ScSiC_2 (M = Ti, V) compositions along with ab initio assessments, *Inorg. Chem. Commun.*, 2024, **167**, 112785, DOI: 10.1016/j.inoche.2024.112785.

50 F. Birch, Finite elastic strain of cubic crystals, *Phys. Rev.*, 1947, **71**, 809–824, DOI: 10.1103/PhysRev.71.809.

51 G. A. Slack, Nonmetallic crystals with high thermal conductivity, *J. Phys. Chem. Solids*, 1973, **34**, 321–335, DOI: 10.1016/0022-3697(73)90092-9.

52 M. E. A. Belhadj, M. Berrahal, A. Bentouaf, M. Belmekki, M. E. A. Elaissaoui El Meliani, F. Benaddi and A. Azzouz Rached, Structural parameters, electronic structure, magnetic and mechanical properties of half-metallic full-Heusler compound Cr_2VAs: a density functional theory study, *Comput. Theor. Chem.*, 2024, **1234**, 114526, DOI: 10.1016/j.comptc.2024.114526.

53 J. E. Saal, S. Kirklin, M. Aykol, B. Meredig and C. Wolverton, Materials design and discovery with high-throughput density functional theory: the Open Quantum Materials Database (OQMD), *JOM*, 2013, **65**, 1501–1509, DOI: 10.1007/s11837-013-0755-4.

54 M. Born, On the stability of crystal lattices. I, *Math. Proc. Cambridge Philos. Soc.*, 1940, **36**, 160–172, DOI: 10.1017/S0305004100017138.

55 Z. Sun, D. Music, R. Ahuja and J. M. Schneider, Theoretical investigation of the bonding and elastic properties of nanolayered ternary nitrides, *Phys. Rev. B:Condens. Matter Mater. Phys.*, 2005, **71**, 193402, DOI: 10.1103/PhysRevB.71.193402.

56 G. V. Sinko and N. A. Smirnov, Ab initio calculations of elastic constants and thermodynamic properties of bcc, fcc, and hcp Al crystals under pressure, *J. Phys.:Condens. Matter*, 2002, **14**, 6989–7005, DOI: 10.1088/0953-8984/14/29/301.

57 D. H. Chung and W. R. Buessem, The Voigt–Reuss–Hill approximation and elastic moduli of polycrystalline MgO, CaF_2, β-ZnS, ZnSe, and CdTe, *J. Appl. Phys.*, 1967, **38**, 2535–2540, DOI: 10.1063/1.1709944.

58 W. Voigt, Lehrbuch der Kristallphysik. Wiesbaden: Vieweg + Teubner Verlag, 1966. Available from: https://link.springer.com/10.1007/978-3-663-15884-4.

59 R. Hill, The elastic behaviour of a crystalline aggregate, *Proc. Phys. Soc., London, Sect. A*, 1952, **65**, 349–354, DOI: 10.1088/0370-1298/65/5/307.

60 X. Q. Chen, H. Niu, D. Li and Y. Li, Modeling hardness of polycrystalline materials and bulk metallic glasses, *Intermetallics.*, 2011, **19**, 1275–1281, DOI: 10.1016/j.intermet.2011.03.026.

61 A. Azzouz-Rached, H. Rached, M. H. M. Babu, T. Hadji and D. Rached, Prediction of double transition metal $(Cr_{1-x}Zr_x)_2AlC$ MAX phases as thermal barrier coatings: insight from density functional theory, *Int. J. Quantum Chem.*, 2021, **121**, e26770, DOI: 10.1002/qua.26770.

62 J. Wang, Y. Zhou, T. Liao and Z. Lin, First-principles prediction of low shear-strain resistance of Al_3BC_3: a metal borocarbide containing short linear BC_2 units, *Appl. Phys. Lett.*, 2006, **89**, 021917, DOI: 10.1063/1.2220549.

63 M. I. A. Tanim, C. Talukder, S. S. Saif, L. H. K. Adnan, N. Jahan and M. M. Hossain, *et al.*, DFT prediction of new o-MAX phases: $Mo_2A_2AlC_3$ (A = Zr, Nb, Ta) for next-generation thermal barrier coatings, *Appl. Mater. Today*, 2026, **48**, 103059, DOI: 10.1016/j.apmt.2025.103059.
64 N. W. Ashcroft and N. D. Mermin, *Solid state physics*, Holt, Rinehart and Winston, Philadelphia, 1976.
65 C. Kittel, *Introduction to solid state physics*, Wiley, Hoboken, 8th edn, 2004.
66 S. Blundell, *Magnetism in condensed matter*, OUP, Oxford, 2001.
67 P. J. Mohr, D. B. Newell, B. N. Taylor and E. Tiesinga, CODATA recommended values of the fundamental physical constants: 2022, *Rev. Mod. Phys.*, 2025, **97**, 025002, DOI: 10.1103/RevModPhys.97.025002.
68 O. L. Anderson, A simplified method for calculating the Debye temperature from elastic constants, *J. Phys. Chem. Solids*, 1963, **24**, 909–917, DOI: 10.1016/0022-3697(63)90067-2.
69 A. Azzouz-Rached, M. Bendjemai, M. Husain, A. Bentouaf, H. Rekab-Djabri, V. Tirth, A. Algahtani, T. Al-Mughanam, A. H. Alghtani, H. Alrobei, M. Elhadi and N. Rahman, Numerical simulation studies of the new quaternary MAX phase as future engineering applications: the case study of the Nb_2ScAC_2 (A = Al, Si) compounds, *Sci. Rep.*, 2023, **13**, 22953, DOI: 10.1038/s41598-023-49172-4.
70 G. K. Arusei, M. Chepkoech, G. O. Amolo and N. Wambua, The elastic properties and lattice dynamics for selected 211 MAX phases: A DFT study [Internet], *arXiv*, 2020, preprint, arXiv:2011.07102, DOI: 10.48550/arXiv.2011.07102.
71 M. Berrabah, T. Cabioc'h, V. Gauthier-Brunet, P. Chartier, E. Epifano and S. Dubois, Synthesis, microstructural characterization and transport properties of a new $(Ti_2Nb)AlC_2$ ternary nanolaminate carbide solid solution, *J. Eur. Ceram. Soc.*, 2026, **46**, 117894, DOI: 10.1016/j.jeurceramsoc.2025.117894.
72 D. R. Clarke and S. R. Phillpot, Thermal barrier coating materials, *Mater. Today*, 2005, **8**, 22–29, DOI: 10.1016/S1369-7021(05)70934-2.
73 Y. Zhou, H. Xiang, X. Lu, Z. Feng and Z. Li, Theoretical prediction on mechanical and thermal properties of a promising thermal barrier material: $Y_4Al_2O_9$, *J. Adv. Ceram.*, 2015, **4**, 83–93, DOI: 10.1007/s40145-015-0140-6.
74 M. E. Fine, L. D. Brown and H. L. Marcus, Elastic constants *versus* melting temperature in metals, *Scr. Metall.*, 1984, **18**, 951–956, DOI: 10.1016/0036-9748(84)90267-9.
75 D. R. Clarke, Materials selection guidelines for low thermal conductivity thermal barrier coatings, *Surf. Coat. Technol.*, 2003, **163–164**, 67–74, DOI: 10.1016/S0257-8972(02)00593-5.
76 T. H. K. Barron and G. K. White, *Heat capacity and thermal expansion at low temperatures*, Springer US, Boston, MA, 1999, DOI: 10.1007/978-1-4615-4695-5.
77 P. Debye, Zur Theorie der spezifischen Wärmen, *Ann. Phys.*, 1912, **344**, 789–839, DOI: 10.1002/andp.19123441404.
78 W. W. Anderson, An analytic expression approximating the Debye heat capacity function, *AIP Adv.*, 2019, **9**, 075108, DOI: 10.1063/1.5110279.
79 N. P. Padture, M. Gell and E. H. Jordan, Thermal Barrier Coatings for Gas-Turbine Engine Applications, *Science*, 2002, **296**, 280–284, DOI: 10.1126/science.1068609.
80 A. G. Evans, D. R. Mumm, J. W. Hutchinson, G. H. Meier and F. S. Pettit, Mechanisms controlling the durability of thermal barrier coatings, *Prog. Mater. Sci.*, 2001, **46**, 505–553, DOI: 10.1016/S0079-6425(00)00020-7.
81 J. Li, J. Jing, J. He, H. Chen and H. Guo, Microstructure evolution and elemental diffusion behavior near the interface of Cr_2AlC and single crystal superalloy DD5 at elevated temperatures, *Mater. Des.*, 2020, **193**, 108776, DOI: 10.1016/j.matdes.2020.108776.